Green Chemistry

Advanced nano-bifunctional electrocatalyst in Li-air batteries for high Coulombic efficiency

Journal:	*Green Chemistry*
Manuscript ID	GC-TRV-06-2023-002151.R4
Article Type:	Tutorial Review
Date Submitted by the Author:	11-Oct-2023
Complete List of Authors:	Zhao, Jinyu; Taiyuan University of Technology Pathak, Rajesh; Argonne National Laboratory Zhao, Zhenxin; Taiyuan University of Technology Chen, Xu; Taiyuan University of Technology Saud, Madan; Syracuse University Li, Hansheng; Syracuse University Wu, Fan; Huzhou University, Qiao, Quinn; Syracuse University, Mechanical and Aerospace Engineering Elam, Jeffrey; Argonne National Laboratory Wang, Xiaomin; Taiyuan University of Technology

Advanced nano-bifunctional electrocatalyst in Li-air batteries for high Coulombic efficiency

[1]Jinyu Zhao□, [2]Rajesh Pathak□*, [1]Zhenxin Zhao, [1]Xu Chen, [3]Madan Bahadur Saud, [3]Hansheng Li, [4]Fan Wu, [3]Quinn Qiao, [2]Jeffrey W Elam*, [1]Xiaomin Wang*

[1] College of Materials Science and Engineering, Taiyuan University of Technology, Taiyuan 030024, China

[2] Applied Materials Division, Argonne National Laboratory, Lemont, IL 60439 USA

[3]Mechanical and Aerospace Engineering, Syracuse University, Syracuse, NY 13244 USA

[4]Department of Applied Physics, Huzhou University, Huzhou,313000, China

□ These authors contributed equally.

E-mails: wangxiaomin@tyut.edu.cn, rpathak@anl.gov, jelam@anl.gov

Abstract:

To meet the growing demand for energy storage technologies, it is crucial to develop next-generation energy storage and conversion devices with superior energy density, safety, low cost, and green sustainability. Li-Air batteries (LABs) can catalyze the special redox reaction of lightweight metal-oxygen (O_2) couples, with superb theoretical energy density, low cost, and environment friendliness, making them suitable for large-scale electricity storage technologies. However, the in-depth understanding of the root causes of poor battery performance and the well-defined electrochemical mechanism based on the structural or material properties is still poor. Hence, we discuss the main obstacles to the sluggish kinetics of oxygen evolution reaction (OER) and oxygen reduction reaction (ORR) at the cathode in LABs in this review. The exploration of special redox reaction based on the catalyst material design is extremely instructive for battery development. Various design/manufacturing methods for nanoscale bifunctional electrocatalysts are introduced to offer general design principles. Electrocatalysts involve alloys, transition metal oxides (manganese-based, cobalt-based), other transition compounds (carbides/nitrides/sulfides), and carbon materials. The effects of different crystal structure designs on the bifunctional electrocatalytic mechanism of OER/ORR are investigated at the nanoscale to guide performance improvement strategies. In addition, the root causes of poor battery performance caused by other components are discussed, as well as their possible future breakthroughs. Finally, the prospects of LABs should be highly focused on an integrated mechanism-structure-property strategy to guide catalyst synthesis and further integration with practical parameters for device development.

Keywords: Li-air battery, Nanoscale material, Bifunctional catalysts, Structure-activity relationships

1. Introduction

The sustained growth in energy demand leads to the excessive consumption of limited non-renewable energy sources, becoming the prime factor for pollution and global warming. It is a strong need to develop next-generation energy storage devices, possessing superior energy density, long-term stability, low cost, and green sustainability.[1-3] The Li-Air battery (LAB) is considered to be the most promising candidate, offering widespread application in electric vehicles and portable electronics due to its ultra-high theoretical specific energy. The LAB concept was introduced in 1976 which within with an alkaline aqueous electrolyte.[4] The first LAB with polyacrylonitrile as electrolyte was reported by Abraham and Jiang in 1996.[5] The discharge capacity, rate and cycling performance of LAB were shown to be dependent on the formulation of the electrolyte and cathode in 2002.[6] Then the electrochemical oxidation of Li_2O_2 was first demonstrated in 2006.[7] By 2008, the outstanding work of the Abraham et al. provided a significant boost to the extensive research on LAB.[8] So far, LABs can be categorized as hybrid, non-aqueous, aqueous, and solid systems, each of which can utilize O_2 from the air efficiently.[9, 10] Particularly, the non-aqueous system enables the highest specific energy density and is considered the safest, cheapest, and more stable in practical applications.

LAB operates based on a unique redox reaction that occurs between the Li metal electrode and O_2 at the air electrode. During discharge of LAB (i.e., oxygen reduction

reaction, ORR), O_2 is reduced by Li ions to form Li (per) oxides by following a reaction: $2Li^+ + O_2 + 2e^- \rightarrow (Li_2O_2)_{solid}$, ($E_{rev}$ = 2.96 V_{Li}). In this step, O_2 combines with one electron and a Li-ion forming a superoxide ion (O_2^-) by following a reaction of $O_2 + Li^+ + e^- \rightarrow LiO_2$. The intermediate LiO_2 is unstable and will fleetly be converted to Li_2O_2 through the chemical route of $2LiO_2 \rightarrow Li_2O_2 + O_2$ or/and $LiO_2 + Li^+ + e^- \rightarrow Li_2O_2$ (electrochemical reduction).[11, 12] The discharge product LiO_2 can increase the theoretical specific energy, however, due to its electrochemical irreversibility, a large charge overpotential is incurred.[13, 14] Thus, the formation of reversible Li_2O_2 not irreversible LiO_2 is highly desirable for improving the performance and efficiency of LAB. Not to be overlooked is the fact that the specifics of ORR can change with variations in the cathode and electrolyte surface states. The oxygen evolution reaction (OER) of LAB in the subsequent charging process follows a reaction as $Li_2O_2 \rightarrow 2Li^+ + O_2 + 2e^-$, ($E_{rev}$=2.96 V_{Li}). The oxidation of Li_2O_2 depends on the microstructure (i.e., crystallinity, morphology) and its parasitic side reaction, influencing the voltage profile.[15] The cathode surface is pivotal in the ORR and OER and dramatically affects the energy storage capacity.

Fundamentally, the full formation and complete decomposition of Li_2O_2 in each cycle is the key to the development of high Coulombic efficiency LAB. The role of the cathode is to afford a framework for realizing the above functions. To allow for Li_2O_2 storage and $O_2/Li^+/e^-$ transport, the cathode must have high specific surface area, three-dimensional open porosity, and superior electrical conductivity.[16, 17] Up to now, many suitable cathodes[8, 18], such as, carbons, precious metals, metal carbides, and metal oxides et al., have been extensively explored and developed by researchers. In addition, although Li_2O_2 has been

shown to be the most desirable discharge product, it still suffers from the disadvantages of insolubility in non-aqueous system and insulation itself.[19] Therefore, Li_2O_2 will gradually be deposited on the cathode surface leading to pore blockage and affecting oxygen transport as ORR/OER proceeds, while an excessively thick deposition layer will limit electron transport. [20, 21] This leads to the fact that the development of only one efficient cathode alone is not sufficient to guarantee the high performance embodiment of LAB. To solve these problems, an efficient bifunctional electrocatalyst needs to be uniformly decorated on the cathode to catalyze the decomposition of residual Li_2O_2 deposited on its surface, thus improving the round-trip OER/ORR efficiency. A series of parasitic side reactions (such as, binder/carbon/electrolyte decomposition) can produce undesired side-products of LiOH and Li_2CO_3 during the ORR/OER process. These substances are insulators and usually cover the surface of the cathode, inactivating the catalytic sites and reducing the cycling efficiency or reversibility of Li_2O_2.[22] It is further revealed that the development of efficient electrocatalysts is crucial for improving the reversibility of Li_2O_2 to enhance the performance of LAB.

Numerous electrocatalysts, including noble metals and their oxides,[23, 24] alloys,[25, 26] transition metal compounds,[27, 28] carbon materials,[29, 30] and soluble redox mediators [31, 32] have been developed to improve round trip efficiency in LAB in the past few decades. In general, noble metals and their oxide have the highest intrinsic activity but high cost; soluble redox mediators can work well as electron-hole carriers to subserve electron transfer between reactants and electrodes, but the catalytic mechanism is more complex. In contrast, alloys, transition metal compounds and carbon materials still occupy a pivotal position in the development of highly efficient bifunctional catalysts due to their advantages of low cost,

easy modification, and relative simplicity of catalytic mechanism. Specifically, alloys can highly circumvent the lateral decomposition channel of oxygen-catalyzed intermediates, improving the long-term operational stability.[33, 34] Transition metal oxides (TMOs) possess a passivating surface layer for accelerating electron transport and restraining parasitic side reactions, enhancing the ORR/OER activity.[35, 36] A thin surface layer of transition metal carbides/nitrides containing a certain percentage of oxygen (O) as potential cathodes can also elevate their thermodynamic stability to achieve reversible Li_2O_2 formation/decomposition.[37, 38] Transition metal sulfides readily complex with carbon materials or other heteroatoms to optimize the oxygen affinity of the surface and thus accelerate the kinetics.[39] Tailoring carbon materials with more defects and abundant mesopores can speed up catalysis and reduces mass transfer resistance.[40]

Thus, a systematic and critical review of the challenges, recent advances, and key results of these bifunctional catalysts for LAB are presented in this paper. The composition control, particle size optimization, morphology control and advanced synthesis strategies are highlighted to further guide the development of efficient ORR/OER catalysts. Besides, the commonly accepted mechanism of LAB is outlined, including a basic understanding of the reaction routes in ORR/OER, as well as the continuing debate over the undesired but ubiquitous parasitic chemistry of the charging process. Furthermore, the root causes of the impact of other components on battery performance are summarized, as well as possible future breakthroughs. Finally, prospective research directions for practical applications of LAB are discussed.

2. The mechanism of ORR and OER of Li-air batteries

Typically, the LAB contains a Li metal anode, electrolyte, separator, and air electrode. The reaction mechanism of LAB has always been controversial. Different studies have attempted to elucidate the underlying chemical reactions that occur within the battery system, using a range of detection methods to identify the key intermediate products and species. Among the proposed reaction mechanisms, the primary reaction is often assumed to be the following reversible process：

$2Li + O_2 \leftrightarrow Li_2O_2(s)$ （E^0=2.96V, vs. Li/Li^+） (1-1)

The discharge reaction is produced in the forward direction (Li_2O_2 is produced by the reduction reaction of O_2, ORR) and the reverse direction is the charging reaction (O_2 is released by the oxidation reaction of Li_2O_2, OER), and so on, thus accomplishing the mutual conversion of chemical energy and electrical energy in the LAB system. [11, 41] Considering the complexity of intermediates (i.e., lithium oxide/mixtures) and the reversibility of Li_2O_2 discharge products, several different reaction mechanisms based on Li_2O_2 formation/decomposition have been proposed.

2.1 **Well-established mechanism of ORR & intermediates**

During the discharge process, molecular oxygen (O_2) undergoes a single-electron reduction at the air cathode interface, resulting in the formation of superoxide (O_2^-) ions, which further forms the LiO_2 discharging product in combination with Li^+ coming from the anode, that is,

$O_2 + e^- + Li^+ \rightarrow LiO_2$ (1-2)

Successively, the formed LiO_2 can accept a second electron or undergo the special disproportionation reaction to form the main Li_2O_2 discharge product, as follows,

$LiO_2 + e + Li^+ \rightarrow Li_2O_2$ (1-3)

or $LiO_2 + LiO_2 \rightarrow Li_2O_2 + O_2$ (1-4)

Notably, there exists an adsorption-dissolution equilibrium at the interface between the electrolyte and the air cathode, which is essential in the O_2 reduction reaction, namely,

$LiO_2^* \rightarrow LiO_{2\,(sol)}$ (1-5)

The "*" here refers to the adsorbed state and "sol" is the dissolved state.

When the solubility of LiO_2 in the electrolyte is low but the absorption energy at the electrode is high, the above reactions (eqs. 1-3 1-4) take place at the electrode surface, which is referred to as the electrode surface growth mechanism. Conversely, the high solubility with low absorption energy of the LiO_2 leads to its dissolution in the electrolyte and the above reactions (eqs. 1-3 1-4), known as the solution growth mechanism. The reduction reaction of $O_2 \rightarrow Li_2O_2$ is a typical two-electron transfer process.

Furthermore, the O_2 can receive not only one or two electrons, but also four electrons to produce Li_2O, corresponding to the four-electron transfer process, as follows,

$O_2 + 4e^- + 4Li^+ \rightarrow 2Li_2O$ (1-6)

This reaction is irreversible and the Li_2O is hard to decompose, which results in high charging overvoltage and is not considered as the main product in the experimental investigations. In summary, for ORR, the single electron transfer is the fastest step in the

kinetic level, so the LiO_2 is the main intermediate product, while the subsequently generated Li_2O_2 is the main discharge product **(Fig. 1)**.

2.2 Elusive mechanism of OER & intermediates

When charging, the theoretical mechanism is that the reverse reaction of Li_2O_2 occurs, resulting in the generation of Li^+, e^-, and O_2. Li^+ then migrates across the separator and through the electrolyte to the anode, where it combines with the e^- flowing from the external circuit to reduce to the metallic Li. Meanwhile O_2 produced during the charging proccess escapes from the system.[42-44] However, the decomposition of Li_2O_2 during charging is greatly affected by various factors such as the type of electrolyte used, the formation mechanism of Li_2O_2 and the morphology of the deposited materials. Also, the side reactions that stem from the electrolyte decomposition can further complicate the charging mechanism. Consequently, the charging reaction mechanism is not fully understood and remains elusive.

Early, Peng et.al.[45] reported the absence of Raman signal corresponding to LiO_2 in the oxidation decomposition process of Li_2O_2, and they proposed that the whole decomposition path for Li_2O_2 follows the direct two-electron reaction at the two-phase interface of itself and the electrolyte:

$$Li_2O_2 \rightarrow 2Li^+ + O_2 + 2e^- \quad (1\text{-}7)$$

When the Li-deficient $Li_{2-x}O_2$ phase as a sort of intermediate was manifested by the operando XRD studies, the researchers deduced that the decomposition process of Li_2O_2 involves two charging regions at different stages.

In the first stage, the amorphous Li_2O_2 is oxidized in the voltage range of 2.8-3.4V with

the removal of Li^+, and some Li^+ vacancies are generated at the Li_2O_2 interface, forming $Li_{2-x}O_2$ with a Li-deficient phase:

$$Li_2O_2 \rightarrow Li_{2-x}O_2 + xLi^+ + xe^- \quad (1\text{-}8)$$

Then, driven by the solid solution reaction of $Li_{2-x}O_2$, the crystalline Li_2O_2 undergoes oxidative decomposition at 3.4-3.9 V and releases O_2:

$$Li_{2-x}O_2 \rightarrow (2-x)\ Li^+ + (2-x)\ e^- + O_2 \quad (1\text{-}9)$$

Another assumption proposed to the charging reaction pathway where the direct diffraction signals of LiO_2 is revealed as the reaction intermediate through in situ transmission electron microscopy (TEM) by was reported by Luo et.al.[46] Further evidence for the indirect presence of LiO_2 intermediates is provided via rotating ring disk electrode (RRDE) measurements by Wang et.al.[47]. In the study, an oxidation current of LiO_2 intermediates was seen at the ring electrode in high donor (DN) solvents such as dimethyl sulfoxide (DMSO). In addition, X-ray absorption near edge structure (XANES) technique provided direct spectroscopic evidence of LiO_2 in high DN solvents, for example, 1-methylimidazole (Me-Im). Based on the above analysis of LiO_2, in the high DN electrolyte, the possible reaction path is as follows:

$$Li_2O_2 \rightarrow LiO_2 + Li^+ + e^- \quad (1\text{-}10)$$

Alternatively, LiO_2 can be produced from the Li-deficient $Li_{2-x}O_2$ phase [81] by:

$$Li_{2-x}O_2 \rightarrow (1-x)\ Li^+ + (1-x)\ e^- + LiO_2 \quad (1\text{-}11)$$

Subsequently, LiO_2 continues to decompose, producing Li^+ and releasing O_2:

$$LiO_2 \rightarrow O_2 + Li^+ + e^- \quad (1\text{-}12)$$

$$\text{(or) } 2LiO_2 \rightarrow Li_2O_2 + O_2 \quad (1\text{-}13)$$

In the charging process, the Li_2O_2 product is a non-soluble and insulating substance, and without the catalyst, the internal product agglomeration is very serious. The decomposition of Li_2O_2 needs to be carried out at a high enough voltage, directly resulting in the low energy conversion efficiency of the LAB, and the organic electrolyte stability at high potentials is poor which eventually causes a rapid decay of the cycling performance.[48]

In summary, for OER, the LiO_2 is also the main intermediate product, finally, the LI_2O_2 undergoes a complete reversible decomposition to release O_2 **(Fig. 1)**.

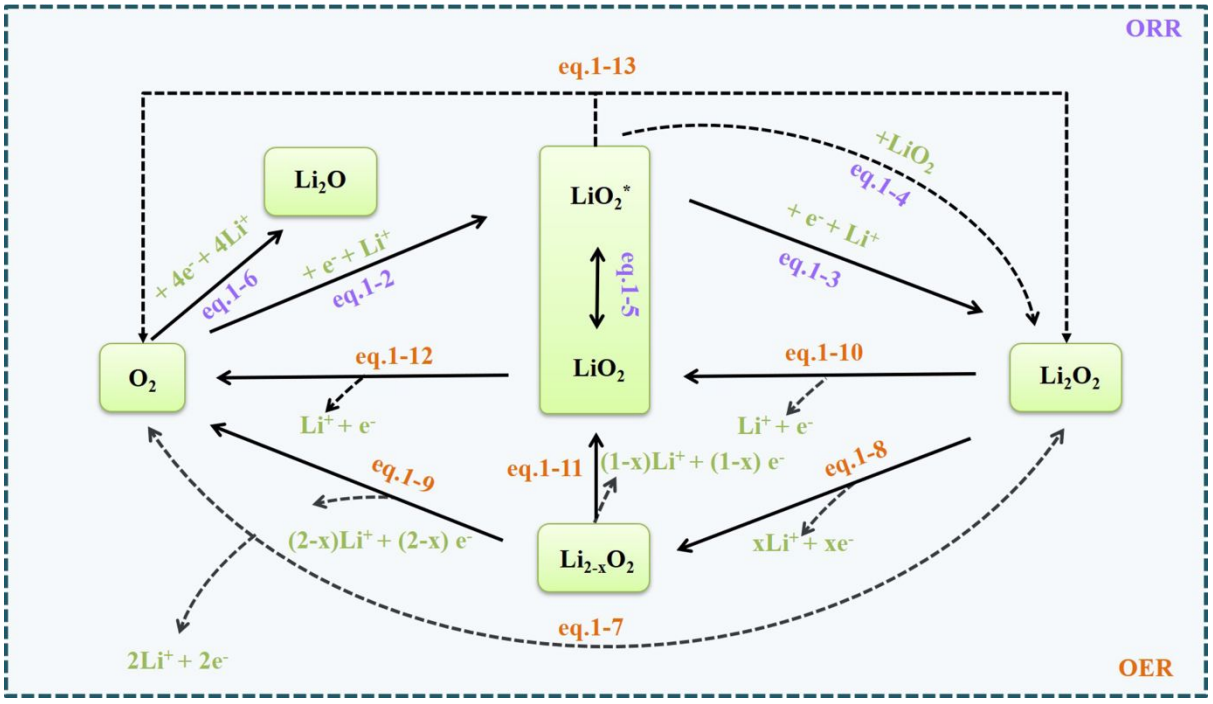

Figure 1 Schematic diagram of the possible ORR and OER mechanisms.

3. Materials design principles of the nanoscale bifunctional catalyst

3.1 Alloys

Alloys with unique properties can be acquired by blending two or more different metals.

When designing alloy catalysts for ORR/OER, it is crucial to determine their usable composition from the possible metal combinations. Based on Sabatier's principle,[49] the reactants, intermediates, and must not bind too weakly or too strongly to the catalyst surface in electrocatalytic reactions[26, 50, 51]. When the binding is too weak, the reaction species do not adsorb well to the catalyst until the end of the catalytic cycle, resulting in a lower overall reaction rate. In turn, too strong binding will promote poisoning of the catalyst surface, blocking more active sites and reducing the reaction rate.

Sevim et al.[52] deposited MPd (M: Co/Ni/Cu) alloy nanoparticles (NPs) onto reduced graphene oxide (rGO) and investigated their electrocatalytic performance for use as catalysts in LAB. A surfactant-assisted organic solution phase method was used to synthesize monodisperse MPd NPs in which Pd(acetylacetonate) and $M(acetate)_2$/ $M(acetylacetonate)_2$ were co-reduced in oleylamine by a boron alkyl mild reducing agent. Subsequently, the liquid self-assembly method was used to load MPd NPs on rGO to obtain efficient and economical electrocatalysts rGO-CuPd, rGO-Co_3Pd_7, and rGO-Ni_3Pd_7. After assembling and testing cells, these catalysts yielded relatively high specific discharge capacities of 4407, 3158, and 2512 mAh g^{-1}, respectively. This further indicated that the variation in the electronic structure of Pd as the LAB cathode with different compositions of Co, Ni, and Cu had a significant impact on the catalytic activity.

In a different study, Leng, et al.[53] developed a series of highly efficient ORR/OER catalysts by anchoring bimetallic PdFe/Co/Ni NPs onto N-doped rGO (N-rGO) for incorporation in LAB. The high surface area of N-rGO promoted the uniform dispersion of alloy NPs **(Fig. 2(a, b))**. Thus, the PdFe/N-rGO showed the best stability, and the cells were

able to cycle stably for 400 cycles at 400 mA g^{-1} under 1000 mAh g^{-1} **(Fig. 2(c))**.

Kang et al.[54] studied the catalytic activity (i.e., ORR/OER overpotentials) of bimetallic Pt_3M (M = 3d/4d/5d transition metals) alloys using first-principles calculations to facilitate the improvement of ORR and OER kinetics. Among them, Pt_3V (3d), Pt_3Nb (4d), and Pt_3Ta (5d) alloys containing group 5 transition metal elements had the highest catalytic activity, as shown by their corresponding ORR and OER overpotentials lower than Pt, 71-77% and 57-59%, respectively. Regarding the highly correlated descriptors of ORR and OER overpotentials, the intermediate (Li and LiO_2) adsorption energies on the surface alloy were appropriate, instead of selecting the energy band centers on their alloy surfaces for characterization **(Fig. 2(d, e))**. Based on this, the excellent catalytic activity of Pt_3M alloys containing group 5 elements was closely related to the electron-rich surfaces, which could also be explained by the integration of mechanical and chemical interactions of Pt and M. It was necessary to ensure a proper balance between the ligand effect and the surface strain.

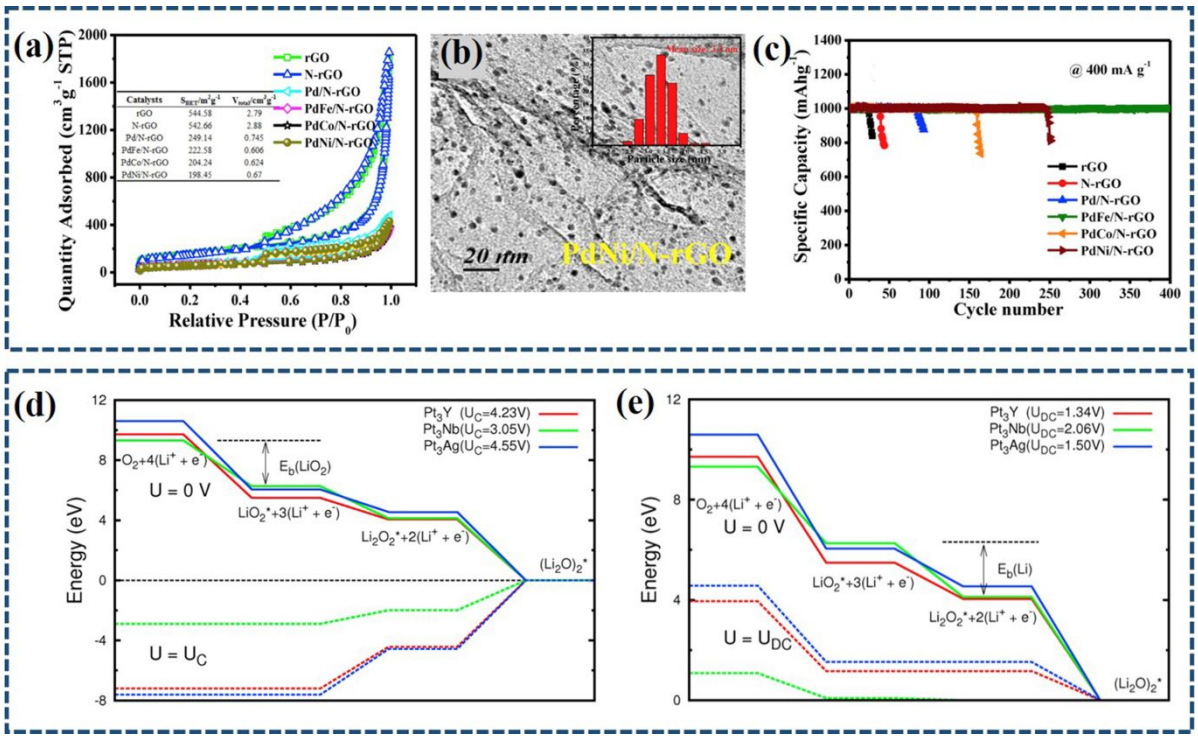

Figure 2 (a) N_2 adsorption/desorption isotherms of Pd(Fe/Co/Ni)/N-rGO catalysts. **(b)** The SEM image of PdNi/N-rGO with the particle size statistics of PdNi NPs. **(c)** Specific capacities of obtained catalysts versus cycle number.[53] Copyright 2016 Elsevier B.V. Calculated energy charts for **(d)** ORR and **(e)** OER on the Pt surfaces of Pt_3Y, Pt_3Nb, and Pt_3Ag. The energies of three reactions with the adsorbed Li_xO_2 (x = 1, 2, and 4) at U = 0 V were colored solid lines; The energy of ORR and OER at U=U_C and U_{DC} were colored dashed lines; The double-headed arrows indicated the LiO_2 and Li adsorption energy in the reaction for the Pt_3Nb at U=0 V.[54] Copyright 2016 Elsevier Ltd.

In addition to composition, the particle size of alloy catalysts affects their electrocatalytic activity. Intuitively, as the alloy particle size decreases, more metal surface area is exposed, increasing the available surface atoms and accelerating the catalytic activity.[55, 56] However, when a certain critical size is reached, the reaction kinetics will no longer increase as the alloy particle size decreases, and may also decrease, at which point it is

no longer appropriate to further reduce the alloy particle size. In addition, when the alloy particle size changes, the number and type of exposed crystalline surfaces will change, and the binding energy of intermediates will depend on the different exposed crystalline surfaces.[57-59] Therefore, precise morphology control and size tuning are essential for the preparation of alloy materials with superior ORR and OER catalytic properties.

Hu et al.[60] prepared well-crystallized PdAu NPs loaded on Ketjen Black (KB) by solution plasma sputtering using metal wire electrodes (i.e., Pd and gold wires as electrode pairs). High-resolution TEM and EDX showed that PdAu NPs with a 2-5 nm average size were uniformly dispersed on the whole KB surface. Further multi-scan cyclic voltammetry results showed that PdAu NPs had better electrochemical stability in alkaline solution (about 700 cycles in NaOH (0.5 M)) than in acidic solution (only about 240 cycles in H_2SO_4 (0.5 M)), compared with KB and Pd+Au/KB.

Lee et al.[61] predicted the electrochemical activity of bimetallic Pt-Cu alloy catalysts in LAB by first-principles calculations. In this work, the study focused on the effect of the atomic ratio of the metal alloy on its intrinsic catalytic performance, excluding the effect of the external environment on the crystalline surface reaction. The free energy figures of Pt (111), Pt_3Cu (111), and PtCu (111) along the ORR/OER pathways shown that the PtCu (111) possessed the lowest charge voltage (U_C) value of 2.73 V, and the highest discharge voltage (U_{DC}) value of 1.99 V **(Fig 3(a-c))**. Further, by analyzing the relationship between the adsorption strength of ORR intermediates on the corresponding alloy crystal surfaces and the charge properties of the alloy surface, it was observed that the PtCu (111) crystal faces were more negatively charged and could serve as weakly positively charged crystal faces for LiO_2

adsorption. This led to a weak ionic bonding of LiO_2 on the PtCu (111) crystal faces, further manifested by a sharp decrease in overpotential. This work reveals that the charge overpotential of alloy catalysts is mainly influenced by the intrinsic surface charge properties, providing a guiding insight for the design of efficient alloy catalysts, which can be expanded to other noble metal-based alloy moieties for the estimation of this catalytic performance.

Alloys synthesized with two-dimensional (2D) nanosheet structures show superior performance in oxygen catalysis when the alloy particle size is adjusted to the sub-nanometer range. Impressively, a highly curved ultrathin PdMo bimetallene nanosheet was prepared by Luo et al.[62] via heating a homogeneous solution of $Pd(Acac)_2$, $Mo(CO)_6$, oleylamine, and ascorbic acid at 80°C for 12 h. The formed 2D sub-nanometer-thick metal alloy nanosheets with a 0.88 nm average thickness, with four atomic layers, were classified as metalloids with a graphene-like structure. Then, this material was deposited on the carbon black to prepare the PdMo bimetallene/C catalyst to test its electrocatalytic. The PdMo bimetallene/C exhibited better ORR/OER activity and durability than RuO_2/C and Pt/C electrodes, which was ascribed to the conjoint effect of quantum size, lattice strain, and alloying effects.

Based on the above analysis, rational design of the microstructure of alloy catalysts, i.e., adjusting the alloy elements distribution in three dimensions (3D) is another effective tactic to improve the catalyst performance.[25, 63] It is also necessary to pay attention to the construction of hierarchical porous structures.

For example, Wang et al.[64] synthesized Fe/Co metal ion organic skeleton MOF by using Fe and $[Co(CN)_6]$ ions as precursors, and subsequently mixed with carbon nanotubes (CNTs) and pyrolyzed at 600 °C to obtain FeCo alloy@NC catalysts with the solid core-shell

structure on CNTs. This special 3D structure was first investigated as a bifunctional electrocatalyst for ORR/OER with a 1.55 V discharge/charge gap and a cycling stability of up to 40 cycles.

Ren et al.[65] designed a novel stand-alone binder-free air electrode using acrylonitrile telomer (ANT) as the dopant and carbon source, and deposited 3D N, S co-doped macro/mesoporous C (NSMmC) on carbon paper (CP) via a template method, followed by uniform coating with PdNi NPs. On one hand, this NSMmC/CP skeleton could afford plenty of space to accommodate the reaction products, and the interconnecting pore channels were also beneficial to promote the diffusion of oxygen and electrolyte. On the other hand, the ultra-fine and uniformly distributed PdNi NPs could offer enough catalytic sites for ORR/OER, which could effectually catalyze the product deposition and decomposition. Therefore, the LAB with PdNi-NSMmC/CP as the catalytic cathode could markedly increase the discharge capacity up to 9965 mA h g^{-1} and reduced the overpotential to 1.05 V.

Recently, Chang et al. [66] prepared a N-doped, C-encapsulated Co-Ni nanoalloy bifunctional catalyst via a bottom-up approach with $Co(NO_3)_2$ and $Ni(NO_3)_2$ as the metal sources and Na_4EDTA as the N-containing C source. The catalyst had a hierarchical architecture **(Fig 3(d))** with a highly dispersed Co-Ni nanoalloy and an ultrathin NC coating layer. DFT calculations **(Fig 3(e))** showed that the coating layer could weaken the O* intermediate adsorption energy on the Co-Ni alloy surface, promoting high OER activity. With 1-3 layers thickness graphene coating layer, the Co-Ni nanoalloy catalyst could exhibit a self-adapted catalytic effect during the cycling, further allowing high stability **(Fig 3(f))**.

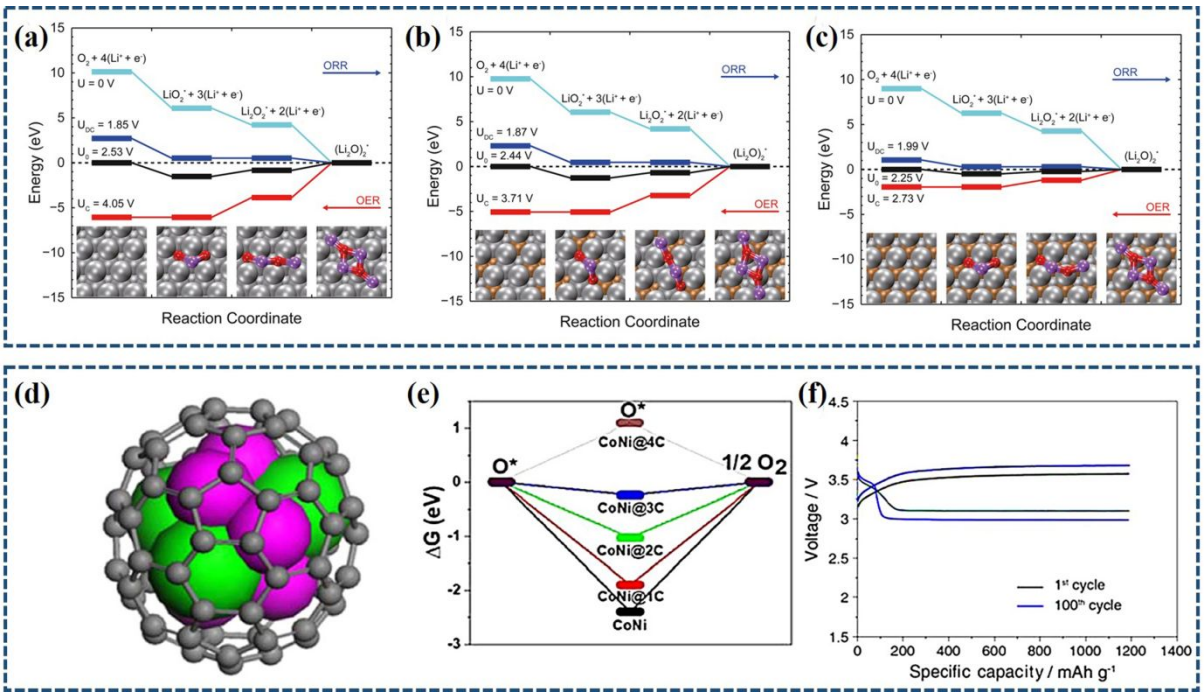

Figure 3 Free energy plots on the surfaces of **(a)** Pt (111), **(b)** Pt_3Cu (111), **(c)** PtCu (111) for the OER/ORR, at U = 0 V/ U_C (minimum) / U_{DC} (maximum) / U_0 (the equilibrium potential), respectively; all with LiO_2, Li_2O_2, and Li_2O_2 as stable adsorption configurations (Purple, Li; red, O; gray, Pt; brown, Cu.).[61] Re-use has been licensed, Copyright 2015 Elsevier B.V. **(d)** Schematic diagram of Co-Ni@C, with C in gray, Co in red, and Ni in green. **(e)** Gibbs free energy (ΔG) profiles of various species on the various catalysts surface during OER; **(f)** The charge and discharge load curves of 1st and 100th cycle at 0.5 mA cm^{-2}.[66] Re-use has been licensed, Copyright 2021 American Chemical Society.

Further to summary, the development of high-efficiency alloy bifunctional catalysts needs to focus on the following points: introducing group V transition metals to induce electron-rich surfaces of noble metals, synthesizing alloy particles with specific particle sizes (2-5 nm), constructing three-dimensional hierarchical porous structures, balancing the ligand effect and the surface strain. The conjoint effect of quantum size, lattice strain, and alloying effects. Tailoring specific integration strategies by modulating the various influencing factors

can ensure the exposure and accessibility of the active sites, which in turn promotes high catalytic activity.

3.2 Transition-metal oxides

Transition-metal oxides (TMOs) have been researched to develop efficient ORR/OER catalysts for optimizing the electrochemical activity of the LABs.[67, 68] As an alternative to precious metals, most TMOs are earth-abundant, low-cost, easy or simple to synthesize, and environmental friendly.[69, 70] In addition, the transition metal elements possess multiple valence states, which is beneficial to the creation of oxides with different crystal structures. [71, 72] In this section, two types of TMO nanomaterials will be discussed based on their synthesis and structure including Mn and Co-oxide based bifunctional catalysts.

3.2.1 Mn-based oxides

Mn-based oxides represent a promising catalyst family for LABs given their rich redox electrochemical characteristics. Manganese dioxide (MnO_2), with bifunctional activity in ORR and OER, is the most widely employed Mn-based oxide, including MnO_2 with different crystal phases and combined with other metals and metal oxides.[73, 74] The octahedron [MnO_6] is the fundamental structural unit of the MnO_2, which can be interlinked with adjacent ones by sharing the corners or edges to form complex lattices that can accommodate various cations or coordinating ions. [75]

The α-, β-, γ- and ε-MnO_2 are one-dimensional (1D) tunneled types structures, differing in the size and arrangement of the tunnels.[76-78] The basic structure unit of α-MnO_2 possesses large (2×2) (0.46nm) and (1×1) (0.189nm) tunnel structures in double-bonded octahedral

chains (corner-sharing). The β-MnO_2 consists of octahedral single chains forming the (1×1) tunnel structure through vertice-sharing, and these small tunnels call for cations to stabilize. The γ-MnO_2 displays irregular (1×1) and (1×2) tunnels surrounded by mono- and di-octahedral chains alternately arranged along the c-axis. Regarding the structure of ε-MnO_2, (1×1) and (2×2) tunnels coexist and the lattice sites of Mn are highly disordered resulting in irregular tunnel shapes and ample structural defects in the ε-MnO_2.

To verify that the catalytic activity of MnO_2 mainly depends on crystal structure, Cheng et al.[79] synthesized a series of α-, β- and γ-MnO_2 with similar diameters and lengths using hydrothermal way to minimize the shape and size effects. In the preparation of α-MnO_2 nanowires (NWs), $MnSO_4 \cdot H_2O$ and $KMnO_4$ were selected as Mn sources, and the hydrothermal way was implemented at 140 ℃ for 12 h. In the preparation of β-MnO_2 NWs, a similar procedure was used, replacing $KMnO_4$ with the equivalent $(NH_4)_2S_2O_8$. By adjusting hydrothermal parameters to 90 °C for 36 h, the transfer from β-MnO_2 to γ-MnO_2 NWs could be realized. The electrochemical properties of the synthesized α-, β- and γ-MnO_2 for ORR in 0.1 M KOH media were measured and the catalytic activities following α->β->γ-MnO_2.

Considerable research has established that oxygen vacancies or structural defects are beneficial catalytic sites for high oxygen electrocatalytic activity. Hence, ε-MnO_2 with richer oxygen vacancies and structural defects than other MnO_2 is extensively employed in ORR and OER due to its unique structural characteristics to suppress overpotentials. Hu and co-workers [80] developed a controllable two-step route for synthesizing the sponge-like hierarchical porous ε-MnO_2 (OTM) in a two-electrode system (Ni foam as a working electrode and Pt foil as a counter electrode) through two steps. Step 1 was to electrolyze

water on the working electrode substrate to produce an oxygen bubble template under the requisite constant current for 10 s. In step 2, nanostructured Mn oxide was electrodeposited on Ni foam with bubble-covered within 0-18 min at a small current of 1.5 mA, then was heated at 350 °C for 1 h in the air to achieve the catalytic material **(Fig 4(a))**. The synthesized ε-MnO_2 electrode exhibited a 0.47 V charge-discharge overpotential, and the cell showed a 5700 mAh g^{-1} discharge capacity at 100 mA g^{-1} and 3400 mAh g^{-1} at 800 mA g^{-1} **(Fig 4(b, c))**. The superior performance is due to the structure of ε-typed MnO_2 enriching with oxygen vacancies and structural defects, as well as the constructed hierarchical porous structure of ε-MnO_2 promotes the reversible conversion reaction of O_2 and Li_2O_2.

The δ-MnO_2 possesses a unique 2D layered structure, creating a higher specific surface area than the other forms of MnO_2 with chain tunnel structure, and its layered structure depends on heterogeneous atoms to occupy its interlayer space for stability. Zhang et al.[81] synthesized the multilayer porous δ-MnO_2 nano boxes via a three-step route using Prussian blue analogs (PBA) as precursors. Specifically, the nanocubic PBA was obtained through the modified self-assembly of reaction reagents ($K_3[Co(CN)_6]$, $Mn(CH_3COO)_2{\cdot}4H_2O$, and polyvinyl pyrrolidone) at room temperature. The synthesis of the intermediate Mn_3O_4 nanoboxes was performed using the precisely controlled reaction of $Mn_3[Co(CN)_6]_2{\cdot}9H_2O$ and NaOH. The final δ-MnO_2 nanoboxes were synthesized by the oxidation reaction of the hollow Mn_3O_4 and $(NH_4)_2S_2O_8$ at 80 °C. The synthetic δ-MnO_2 possessed a 249.3 m^2 g^{-1} surface area and a hierarchy of pore sizes which were advantageous for the delivery of O_2 and could furnish more catalytic active sites to facilitate ORR and OER. It exhibited the discharge capacity of 4368 mA h g^{-1} at 0.08 mA cm^{-2} and the cycle stability of 112 cycles with 1000

mA h g^{-1} at 0.16 mA cm^{-2}.

Recently, the high active δ-MnO_2 was used as a coating layer on various carbon carriers to enhance the catalytic activity of the bifunctional catalysts. For example, Hu et. al [82] coated 2-3 nm thick δ-MnO_2 on multi-walled carbon nanotubes (MWCNTs) as cathode catalysts for LAB. The special nanocomposite catalysts promoted the decomposition of Li_2O_2 and avoided some side reactions **(Fig 4(d))**. Notably, they integrated this catalyst with the N,N′-bis(salicylidene)ethylenediaminocobalt(II) (Co^{II}-salen) electrolyte (i.e., a mobile O_2-carrier) to accelerate O_2 transfer to facilitate the Li_2O_2 formation **(Fig 4(e))**. This accelerated reaction overcame the limitations of the pure O_2, which were more applicable for the air cathode in LAB. The novel Co-salen/MCNTs@δ-MnO_2 catalyst showed a long lifetime allowing 300 cycles under 500 mA g^{-1} (0.15 mA cm^{-2}) with 1000 mAh g^{-1} (0.30 mAh cm^{-2}) fixed capacity and showed a steady terminal voltage of about 2.80 V after 300 cycles discharge **(Fig 4(f))**.

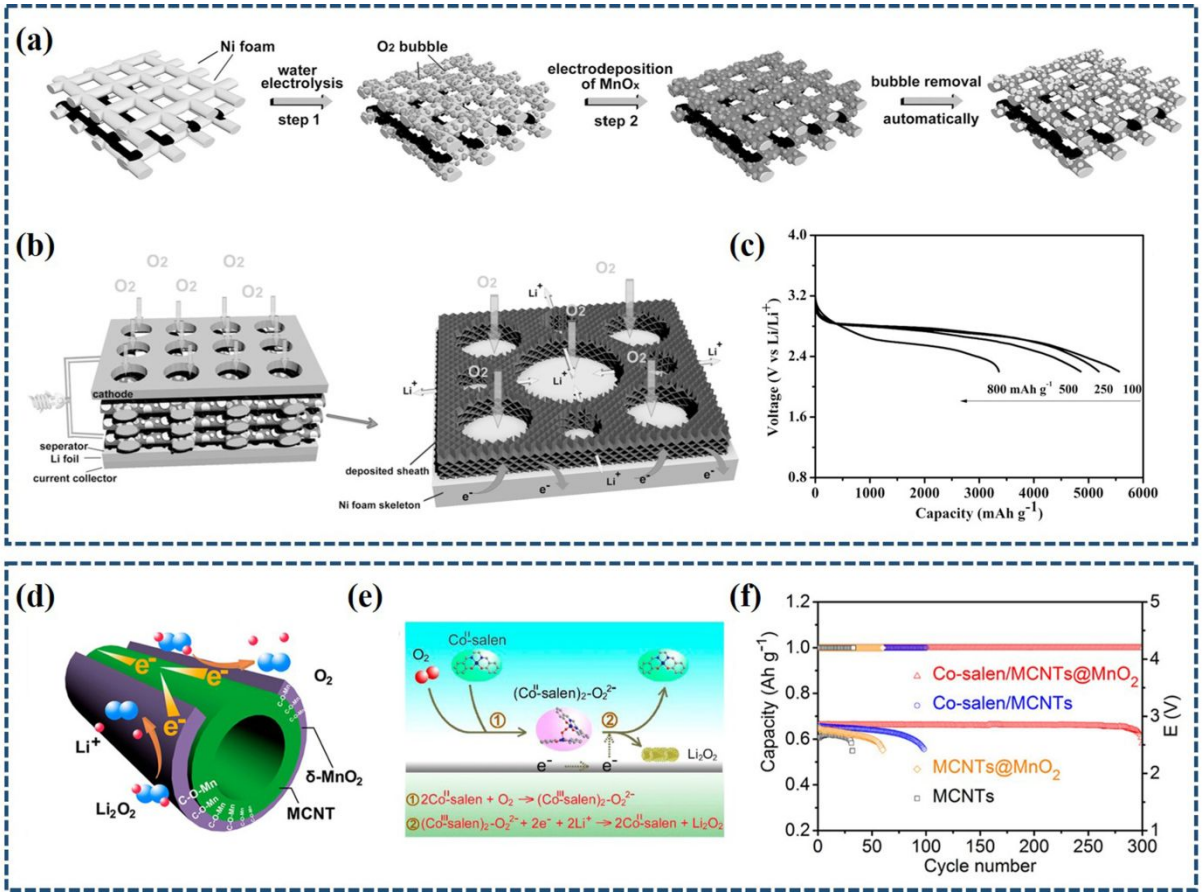

Figure 4 Sketch map for OTM of **(a)** its preparation and **(b)** its advantageous application in LAB; **(c)** Rate performance of OTM cathode-based LAB;[80] Copyright 2015 WILEY-VCH Verbg GmbH&Co. KGaA, Weinheim. **(d)** Sketch map of the Li_2O_2 decomposition on MCNTs@δ-MnO_2 surface; **(e)** Sketch map of the accelerated reaction mechanism in LAB with Co^{II}-salen as electrolyte; **(f)** Cyclability of Co-salen/MCNTs@δ-MnO_2 at 500 mA g^{-1} (0.15 mA cm^{-2}) with a 1000 mAh g^{-1} capacity (0.30 mAh cm^{-2}). [82] Copyright 2017 American Chemical Society.

Pure MnO_2 was shown to have relatively excellent performance, and crystal structure, oxygen vacancies, structural defects, and multilayer porosity were also shown to be key factors affecting its electrocatalytic performance. Although the special structural characteristics of each pure MnO_2 have contributed to its excellent performance, a high OER

overpotential still exists during discharging/charging. Thus, MnO_2-based bifunctional catalysts have been designed for further lower the charge potential by incorporating noble metals and their oxides or other transition metal oxides. [83-85]

For example, noble metal Pd decorated mesoporous α-MnO_2 nanotubes (α-MnO_2/Pd) were synthesized by Thapa et al.[86]. Firstly, the $KMnO_4$ was reduced in an acidic medium followed by sequential proton and alkali ion exchange to prepare the α-MnO_2, which had rich mesoporous structure after this process **(Fig 5(a))**. Then the mixture of Pd, mesoporous α-MnO_2, and teflonized acetylene black (TAB), at a ratio of 75:15:10, was used for the cathode. The cathode showed the stabilized discharge-specific capacity of 261 and 212 mAh g^{-1} after 15 cycles, at 0.25 and 1.91 $mAcm^{-2}$, respectively **(Fig 5(b))**, which is due to the synergistic catalytic effect of Pd and α-MnO_2. In their subsequent work,[87] the Au-Pd nanoparticle modified mesoporous β-MnO_2 composites (β-MnO_2/Au-Pd) **(Fig 5(c))** as a cathode catalyst with accelerated ORR/OER kinetics was reported. To synthesize β-MnO_2/Au-Pd, a mixture of $HAuCl_4$, $PdCl_2$, $Mn(NO_3)_2$ was reacted hydrothermally, with silica KIT-6 as the template. The discharge capacity of the cathode had improved to 775 mAh g^{-1} at 0.13 mA cm^{-2}, which is owing to Au-Pd and α-MnO_2 synergistically catalyzing the Li_2O_2 decomposition **(Fig 5(d))**.

In view of the efficient synergistic catalytic contribution of noble metal Pd, some prominent works have also been devoted to the deposition of Pd on MnO_x. For example, Oh et al.[88] assembled Pd decorated MnO_x catalysts through a facile and moderate chemical reaction with the M13 virus as a biological template. The bio-template contributed to the successful synthesis of MnO_x nanowires with high aspect ratios (bio-MO nanowires), which were subsequently encapsulated with only 3 wt% Pd to show excellent performance. As the

high aspect ratio Pd/bio-MO nanowires form a porous network, the interaction between the discharge product (Li_2O_2) and the catalyst was maximized, thus yielding a specific capacity of 7340 mAh g^{-1}at 0.4 A g^{-1} and a cycle life of 50 cycles with 400 mAh g^{-1} at 0.4 A g^{-1}.

Noble metal modified MnO_2 catalysts are always combined with carbon carriers to enhance the dispersion to enhance their catalytic activity in LAB. For example, Alaf et al. [89] used $KMnO_4$ and H_2PtCl_6 as the Mn and Pt sources to produce Pt NPs modified α-MnO_2 catalyst via direct reduction way. Next, a free-standing α-MnO_2/Pt/graphene-MWCNTs catalyst was prepared via vacuum filtration. Notably, the incorporation of multi-wall carbon nano tubes (MWCNTs) in graphene avoided flake aggregation and increased the separation between the two layers **(Figure 4(e))**. The superior modified graphene carriers contributed to the uniform α-MnO_2 and Pt dispersion. The novel heterogeneous catalysts showed excellent ORR/OER activity for LAB. The discharge capacity remained above 560 mAh g^{-1} even after 10 cycles at 0.01 mA cm^{-2}**(Fig 5(f))**.

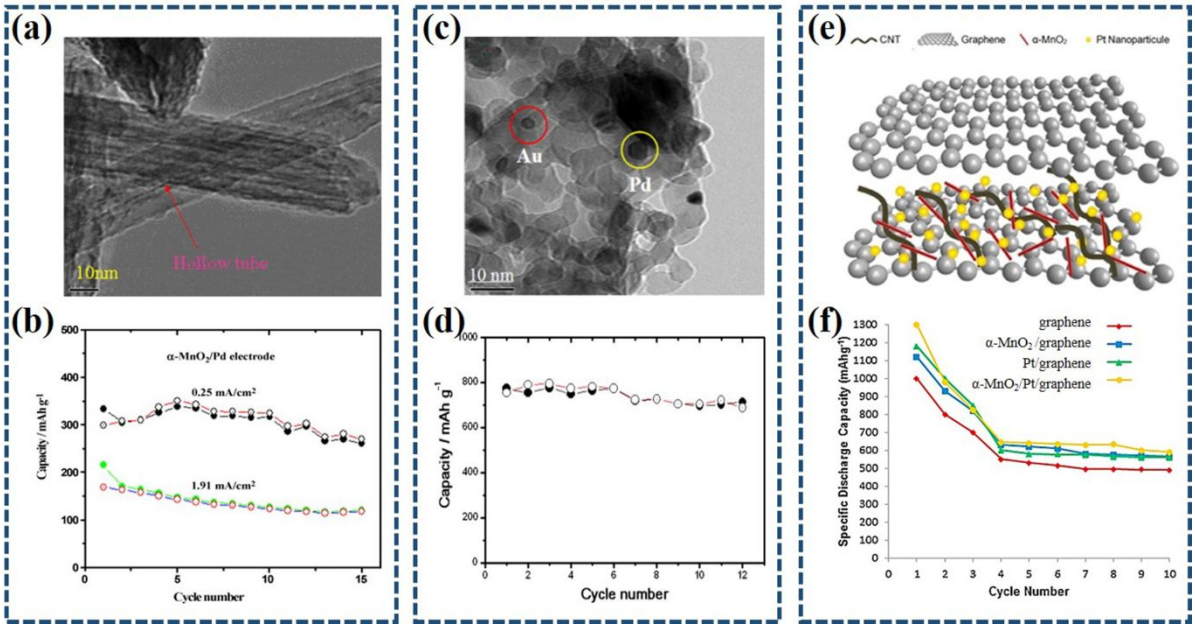

Figure 5 (a) TEM pattern of α-MnO_2 (mesoporous); **(b)** The correlation of charge/discharge capacities and cycle for Pd/mesoporous α-MnO_2/TAB (15/75/10) electrode at 0.25 and 1.91 $mAcm^{-2}$.[86] Reused with approval; Copyright 2010 Elsevier. B.V. **(c)** TEM pattern and **(d)** The correlation of charge/discharge capacities and cycle for β-MnO_2/Au-Pd at 0.13 mA cm^{-2}.[87] Copyright 2012 Elsevier. B.V. **(e)** Schematic presentation of the obtained α-MnO_2/Pt/graphene-MWCNTs catalysts; **(f)** Cycling performance of the α-MnO_2/Pt/graphene-MWCNTs catalysts, with graphene, Pt/graphene, and α-MnO_2/graphene, for comparison. [89] Copyright 2020 Elsevier. B.V.

For the study modifying MnO_2 with noble metal oxides, Jang et al.[90] developed a 3D sea urchin shaped α-MnO_2/RuO_2 catalyst through a simple hydrothermal process in the early stage. The mixed oxides consisted of multiple straight and radially grown nanorods with uniformly distributed MnO_2 and RuO_2 NPs. The mixed oxide could be stable up to 50 cycles with 500 mAh g^{-1} at 0.1 mA cm^{-2}. The catalytic activity of α-MnO_2/RuO_2 is also significant increased compared to α-MnO_2. Both might be due to the excellent ORR performance of α-MnO_2 and prominent OER activity originating from RuO_2.

Similarly, Xu et al.[91] proved that MnO_2 nanorods uniformly decorated with RuO_2 nanoparticles (nr-MnO_2/np-RuO_2) exhibited promising bifunctional catalytic activity for ORR and OER. It shows a 500 mAh g^{-1} reversible capacity at 50 mA g^{-1} after 75 cycles and even a higher capacity of 4000 mA h g^{-1} at 200 mA g^{-1} after 20 cycles. A facile hydrothermal treatment of $KMnO_4$ and $MnSO_4$ at 180 °C for 10 h was to create the β-MnO_2, and then add $RuCl_3$, followed by ultrasonic and hydrothermal treatment to form the final products. In situ XRD and ex situ SEM images illustrated that this composite catalyst enabled Li_2O_2 formation and decomposition.

From the above works of Jang[90] and Xu[91], it shows that RuO_2 has outstanding potential for catalyzing ORR and OER. Due to the scarce and expensive of Ru, the direct development of pure RuO_2 is not desirable and it is essential to adjust its intrinsic structure to maximize the active sites. In this regard, Dou et al.[92] developed carbon nanotubes supported amorphous RuO_2 nanoparticles catalyst (A-RuO_2@CNT) for LAB. The obtained catalyst exhibited the disordered structure and enriched in oxygen vacancies, which regulated the nucleation and growth of Li_2O_2 into amorphous membranous forms, thereby decreasing the overpotential (0.46 V). This special Li_2O_2 achieved high ionic/electronic conductivity and low interfacial impedance, thus improving battery reversibility, with a stable cycling of 173 cycles with 1000 mA h g^{-1} at 300 mA g^{-1}. These indicated that customizing amorphous RuO_2 is a good way to improve the efficiency of bifunctional catalysis.

In addition to RuO_2, several works have been devoted to the modification of MnO_2 using other noble metal oxides. Recently, Tang et al.[93] proposed a novel binder-free catalytic cathode including 2D δ-MnO_2 (5-10 nm) with small-sized IrO_2 NPs (5 nm). A simple two-step hydrothermal approach was used to grow IrO_2/δ-MnO_2 directly on carbon cloth, where the 2D δ-MnO_2 with interwoven structure was composed of nanoflakes vertically grown on carbon fibers and nanoribbons on the flake surfaces. The 2D IrO_2/δ-MnO_2 catalyst with numerous catalytic sites catalyzed the conformal growth of amorphous Li_2O_2 on its surface **(Fig 6(a))**, and the battery delivered an ultrahigh 16370 mAh g^{-1} reversible capacity at 200 mA g^{-1} **(Fig 6(b))**.

Modifying MnO_2 with noble metals and their oxides can enhance catalytic performance mainly due to the synergistic effect of the two components. The morphology, dispersion, and

pore structure have also been examined as the key factors affecting the performance of such catalysts. That is, the 3D special morphology or other interwoven structure, and high dispersion of two catalytic components provides enough active sites. The 3D open structure and the hierarchical porous especially with rich mesoporous of the modified MnO_2 catalysts ensures the passage of reactant molecules and the accessibility of active sites.

Besides, more study focus on two-component transition metal oxides, including transition metal oxides modifying MnO_2. Wang et al.[94] reported a catalyst combining Co_3O_4 NPs (5 nm) with α-MnO_2 nanowires (5-20 nm in diameter, 5-10 mm in length) (α-MnO_2/Co_3O_4), which was prepared by a two-step hydrothermal process. The synergistic and interfacial effects between the α-MnO_2 and Co_3O_4 formed oxygen vacancies on the α-MnO_2 surface, and these oxygen defects promoted O_2 adsorption and O-O bond dissociation and yielded a high-capacity of 1000 mA h g^{-1} after 60 cycles at 0.1 mA cm^{-2}.

Additionally, Cao et al.[95] has successfully prepared a 3D porous structure CeO_2/δ-MnO_2 catalyst consisting of 2D graphene-like δ-MnO_2 and ultrafine CeO_2 NPs on the surface. The catalyst was prepared by a hydrothermal method using $Ce(NO_3)_3$ as the Ce source and Ni/G foam as the substrate, and a $NaHCO_3$ aqueous solution to adjust the pH. For the CeO_2/δ-MnO_2 electrode, Li_2O_2 grew into hyperfine nanoparticles that loosely accumulate on the CeO_2-modified/δ-MnO_2 surface facilitated reaction accessibility, and CeO_2 acted as a catalyst owing to its strong binding ability to reactive O_2 and LiO_2. Consequently, the assembled LABs demonstrated stable 296 cycling stability with 500 mA h g^{-1} at 100 mA g^{-1}.

Recently, the urchin-like Co_3O_4 was grown by Li et.al, [96] using hydrothermal processing on flexible carbon cloth (CC). Following the reduction reaction of MnO_4^- under acidic

conditions, Co_3O_4@MnO_2@CC catalyst with 3D open structure (3DOS-Co@Mn@CC) was prepared again via a secondary hydrothermal treatment. This catalyst-integrated cathode showed superior ORR/OER activity owing to the 3D open structure of Co_3O_4@MnO_2, and with good mechanical flexibility imparted by the flexible CC. The flexible cathodes containing 3DOS-Co@Mn@CC bifunctional catalyst were further integrated with a Li metal anode and gel electrolyte to form a flexible LAB (gel-CLA-DCs LAB). This LAB demonstrated more than 100 cycles with 500 mA h g^{-1} at 500 mA g^{-1} at an operating environment of 50% relative humidity **(Fig 6(c, d))**.

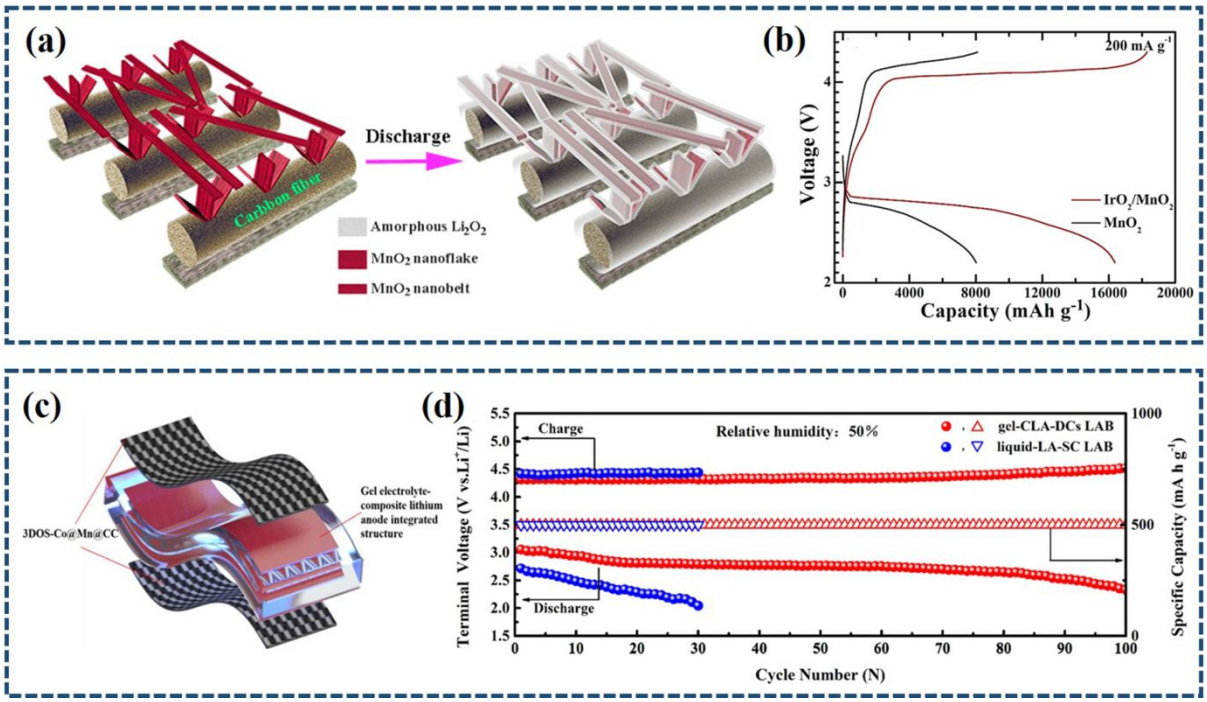

Figure 6 (a) Schematic of the IrO_2/δ-MnO_2 cathode with the working mechanism; **(b)** The relative voltage profiles at 200 mA g^{-1};[93] Reused with approval; Copyright 2020 Elsevier. B.V. **(c)** Sketch map of the integrated flexible gel-CLA-DCs LAB; **(d)** The plots of terminal voltage and discharge-charge capacity versus the cycle number.[96] Re-use has been licensed; Copyright 2021 American Chemical Society.

The above work shows that the surface modification of MnO_2 by transition metal oxide nanoparticles facilitates both adsorption and dissociation of reactive oxygen species and the formation of nanoscale, loosely packed, large surface area Li_2O_2, which makes it easy to decompose thus reducing or delaying electrode passivation. Besides, the 3D open porous structure is necessary to facilitate mass-transfer. The oxygen vacancies formed in the catalyst are reaffirmed to favor bifunctional catalysis. These two points also apply to the development of other efficient two-component transition metal oxide catalysts. For example, He et al. [97] developed 3D-architecture NiFeO cubic spine for LAB with a high capacity of 23413 mAh g^{-1} at 100 mA g^{-1} and a desirable cyclability of 193 cycles with 1000 mAh g^{-1} at 1000 mA g^{-1}. The excellent performance was attributed to the NiFeO featuring porous frameworks and abundant channels to accommodate Li_2O_2 and facilitate species transport. Meanwhile, the oxygen vacancies (corresponding to low-coordinated Fe^{3+} atoms) on the NiFeO surface accelerated the catalytic activity of OER and ensured the battery reversibility.

3.2.2 Co-based oxides

Cobalt oxide (CoO_x) is another outstanding candidate for ORR/OER catalysts in LAB given its tunable composition and superior electrocatalytic activity, especially Co_3O_4. For Co_3O_4, Co^{2+}, and Co^{3+} ions typically coexist and occupy tetrahedral and octahedral sites, respectively.[98-100] The cobalt ions with different valence states (Co^{2+} and Co^{3+}) result in the bifunctionality of ORR/OER, which is a reversible adsorption-desorption of O_2 by acting as a donor-acceptor chemisorption site. Menezeset et al.[101] reported porous materials prepared by thermal degradation of the respective carbonate precursors ($Co_{0.33}Mn_{0.67}CO_3$ and

$Mn_{0.33}Co_{0.67}CO_3$) at 400℃ in air. They found that the reduction of ions in the octahedral position (Co^{3+}) had an adverse effect on oxygen release, remarkably, in ORR, the opposite is true, i.e., the ORR activity and stability of the tetragonal $CoMn_2O_4$ catalyst was better than that of the cubic $MnCo_2O_4$ catalyst. Therefore, the Co^{2+} and Co^{3+} active sites on Co_3O_4 needed to be exposed, and the optimal ratio of Co^{2+}/Co^{3+} active sites with their surface atomic arrangement should be carefully controlled to maximize the ORR/OER activity.

The porosity of Co_3O_4-type monometallic oxide catalysts also facilitates continuous gas supply and mass transfer to the electrolyte in operation. For instance, a new concept of a carbon-free cathode design was introduced by Cui et al.[102] They reported a free-standing rechargeable LAB cathode consisting of Ni foam with Co_3O_4 nano-rods deposited on its surface (Co_3O_4@Ni) prepared using a simple chemical deposition reaction. The 3D network structures and holes provided favorable paths for the diffusion of O_2 and Li^+, with good electronic connection between the Ni collector and rods. The new air electrode showed a 4000 mAh g^{-1} specific capacity with a potential gap of 0.49 V_{Li+} at 0.02 mA cm^{-2}. Sa et al.[103] prepared ordered mesoporous Co_3O_4 as catalysts for ORR/OER using a conventional hydrothermal method with KIT-6 as a template. Regulating metal oxides into mesoscopic structures was an effective method for the development of highly active and stable catalysts, and the total over-potential of the meso-Co_3O_4 phase was 1.03 V.

The incorporation of noble metals nanoparticles is another efficient strategy to improve the Co_3O_4 activity, which can reduce the reaction overpotential, side reactions, etc. In the work of Cao et al.[104], the co-catalytic effect of fixed Co_3O_4 nanowire arrays (NAs) and mobile Pd nanocrystals (NCs) was used to achieve a high-performance of LAB with 5337

mAh g^{-1} discharge capacity that remained stable for more than 250 cycles at 100 mA g^{-1}**(Fig 7(a))**. The co-catalytic effect came from the fact that Pd NPs in the electrolyte catalyzed the conformal Li_2O_2 growth on Co_3O_4 nanowires **(Fig 7(b))**. To prepare the Co_3O_4@Pd, the octahedral Pd (10-20 nm) obtained by a traditional chemical method was dissolved in the electrolyte to form Pd NCs as the liquid portion, and Co_3O_4 NAs were grown directly on the Ni substrate by a facile hydrothermal way with annealing treatment as carbon/binder-free solid portion.

Similarly, Amin et al.[105] developed a carbon-free oxygen electrode with a catalyst that combined the high OER activity of Co_3O_4 and the high ORR activity of Ag. The mixed catalyst consisted of 10 wt% spinel Co_3O_4 NPs (50nm diameter) and the silver microparticles (Ag311). It was hypothesized that due to the presence of Ag^+, Co_3O_4 could be reduced to $Co(OH)_2$ at the potential of the ORR after oxidation of the mixed catalyst. The ORR activity remaining 12% free Ag sites was higher than that of the pure Ag surface (100%) when 88% of the Ag surface was covered by Co_3O_4 particles, at which point the activity of each Ag site was increased by more than 10 times. The material exhibited bifunctional activity in alkaline media, i.e., a potential difference of 0.85 V between OER and ORR, which was comparable to that of noble metal-based catalysts.

An alternative strategy is to use simultaneous reduction methods wherein surface, interface, and doping engineering can create better activity than loading noble metal particles onto self-supporting Co_3O_4 electrodes as described above. Gao et al.[106] proposed a facile simultaneous reduction route to prepare egg yolk shell Co_3O_4@Co_3O_4/Ag catalysts **(Fig 7(c))**. In this method, $K_3[Co(CN)_6]$, $Co(NO_3)_2 \cdot 6H_2O$, sodium dodecyl sulfate (SDS), and silver

nitrate were gradually mixed and reacted at room temperature to obtain a pink precipitate, and then annealed to obtain the end product. For the hybrid materials, part of the Ag formed single atoms or clusters on the Co_3O_4 shell layer surface, strengthening the bonding at the Ag-Co_3O_4 interface. Another part of the Ag was doped into the Co_3O_4 lattice to adjust the valence electron structure of Ag and Co thereby improving the electrical conductivity. In addition, the introduction of Ag caused the Li_2O_2 to deposit with a flower-like morphology on Co_3O_4@Co_3O_4/Ag-based cathodes during the ORR process and decomposed more easily **(Fig 7(d))**. This special structure offered more active centers for ORR/OER, and yielded a high initial capacity of 12000 mAh g^{-1} at 200 mA g^{-1} **(Fig 7(e))**, even a high capacity of 4700 mAh g^{-1} at 800 mA g^{-1}.

Unique Co_3O_4 nanostructures have been investigated to improve the ORR/OER activity for LAB. For example, Li et al. [107] adopted Co_3O_4-nanorods to entangle carbonizing polyaniline nanotubes (Co_3O_4-e-cPANI) and provided dual catalytic performance. This catalyst was synthesized using hydrothermal way with $CoCl_2 \cdot 6H_2O$ as Co sources for Co_3O_4-nanorods. The integrated hierarchical structure **(Fig 7(f))** improved the O_2 diffusion and electrolyte penetration and yielded high activity in catalyzing the Li_2O_2 decomposition. Additionally, the unique conductive network of cPANI promoted facile electron transport and avoided the low conductivity obstacle of the high-active Co_3O_4. In conclusion, LAB with the Co_3O_4-e-cPANI bifunctional catalyst exhibited a superior 32478.3 mAh g^{-1} discharge-specific capacity at 100 mA g^{-1}, as well as a long cycle life of 226 cycles with 500 mAh g^{-1} at 300 mA g^{-1}. **(Fig 7(g))**

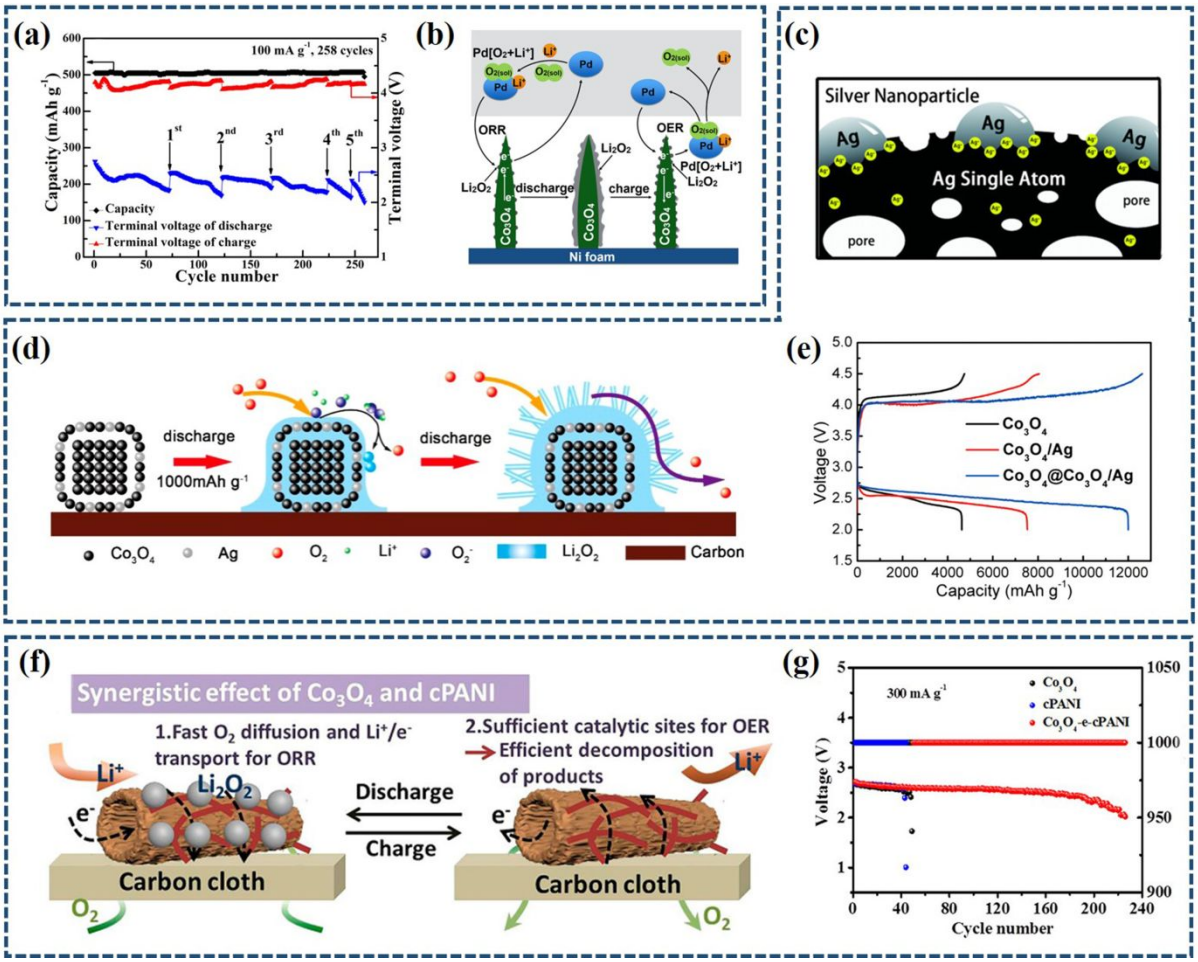

Figure 7 (a) Terminal voltages curves of Li-Co_3O_4NA cells at 100 mA g^{-1}; **(b)** Sketch map for microstructure and catalytic mechanism of Co_3O_4@Pd electrode;[104] Copyright 2016 American Chemical Society. **(c)** Diagrammatic drawing for the Co_3O_4@Co_3O_4/Ag microstructure; **(d)** Possible mechanism for Li_2O_2 on Co_3O_4@Co_3O_4/Ag catalysis; **(e)** The capacity and cycle performance of Co_3O_4-, Co_3O_4/Ag-, and Co_3O_4@Co_3O_4/Ag-based cathodes measured at 200 mA g^{-1};[106] Re-use has been licensed; Copyright 2018 American Chemical Society. **(f)** Schematic diagram of the formation and decomposition mechanisms of Li_2O_2 during ORR/OER on the Co_3O_4-e-cPANI surface; **(g)** The stabilities of the LAB with Co_3O_4, cPANI, and Co_3O_4-e-cPANI as the cathodes at 300 mA g^{-1}, with a limited capacity of 1000 mAh g^{-1}. [107] Copyright 2019 American Chemical Society.

Another desirable attribute of Co_3O_4 as an electrocatalyst is that this spinel-type oxide

can easily accommodate different kinds of transition metals (M= Ni, Mn, Cu) into the lattice. These binary MCo_2O_4 oxides have better electronic conductivity and higher electrochemical activity than the single-component metal oxides. Thus, Co_3O_4 has been extensively researched as a bifunctional catalyst for ORR and OER of LAB.[108, 109] For instance, Peng et al.[110] synthesized 3D multilayered $NiCo_2O_4$ core-shell microspheres composed of porous nanosheets **(Fig 8(a))**, which supplied a high density of catalytic sites and facilitated the flow of O_2 electrolyte penetration ultimately improving catalytic activity. This efficient 3D electrocatalyst was synthesized by solvothermal synthesis combining $Ni(NO_3)_2$ $6H_2O$ and $Co(NO_3)_2$ $6H_2O$ at 200℃ for 10 h. The 3D layered $NiCo_2O_4$ catalysts assembled into LAB exhibited excellent specific capacity of 6822 mA h g^{-1} at 200 mA g^{-1} and showed excellently stable capacity of 1000 mA h g^{-1} after 128 cycles at 200 mA g^{-1} **(Fig 8(b))**.

Hierarchical porous 3D $MnCo_2O_4$ nanowire bundles (W-MCO-NWB) were grown directly on acid-treated nickel foam nets using a versatile, low-cost, and efficient hydrothermal method by Wu et al.[111], using Mn $(NO_3)_2{\cdot}4H_2O$ and Co $(NO_3)_2{\cdot}6H_2O$ **(Fig 8(c))**. The composite $MnCo_2O_4$ electrode with a hierarchical interconnected mesoporous/macro-porous structure reduced the O_2 diffusion path, facilitated electron transport, and improved the electrode conductivity. This carbon-free, binder-free material was used as the cathode catalyst for the LAB and the W-MCO-NWB-based battery system exhibited a 12919 mAh g^{-1} reversible capacity at 0.1 mA cm^{-2} and the cycling performance could be maintained for more than 300 cycles with 500 mAh g^{-1} at 0.1 mA cm^{-2} **(Fig 8(d, e))**. More importantly, the microstructure of the hierarchical porous 3D mesh self-supporting electrode remained almost unchanged after two months of cycling, making the LAB highly

stable.

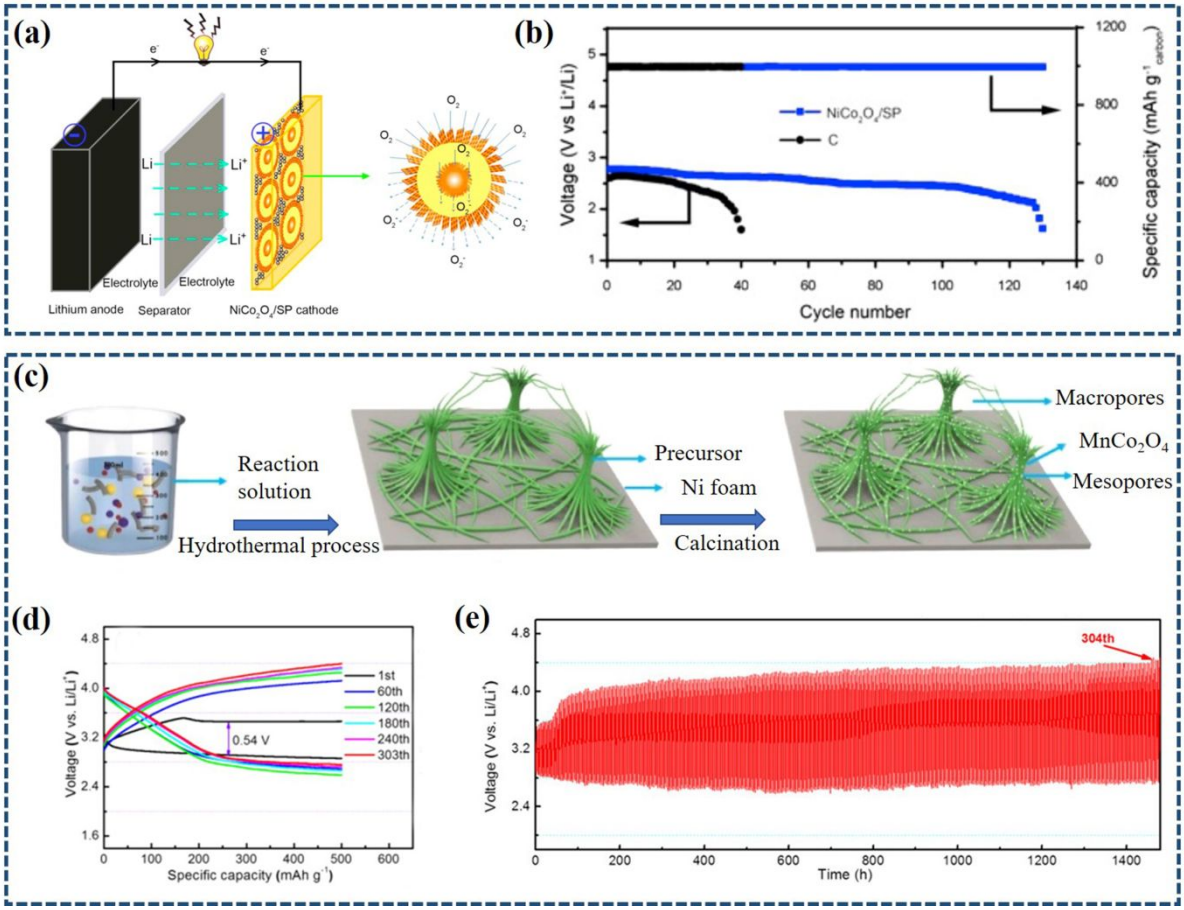

Figure 8 (a) Representative sketch map of a 3D $NiCo_2O_4$ core-shell microsphere catalyst catalyzed LAB; **(b)** Terminal voltages and cycle number curves of LAB at 200 mA g^{-1};[110] Re-use has been licensed; Copyright 2015 Elsevier Ltd. **(c)** Schematic illustration of hierarchical porous 3D $MnCo_2O_4$ on Ni foam; **(d)** The galvanostatic cycling curves of W-MCO-NWB based LAB at 0.1 mA cm^{-2} and **(e)** corresponding stability curve;[111] Re-use has been licensed; Copyright 2017 American Chemical Society.

Mohamed et al.[112] assessed the effect of replacing toxic Co^{2+} on the catalytic activity of LAB cathodes by choosing environmentally friendly transition metals (Mn^{2+}, Fe^{2+}, Ni^{2+}, Zn^{2+}) to substitute the tetrahedral spinel A-site ions. In the facile hydrothermal synthesis of $MnCo_2O_4$, $FeCo_2O_4$, $NiCo_2O_4$, and $ZnCo_2O_4$ nanorods, the corresponding metal nitrates were

dissolved in deionized water and cobalt nitrate and heated to 140°C for 7 h. The resulting series of MCo_2O_4 nanorods, with porous structure, facilitated the flow of O_2 and electrolyte in the ORR, thus providing a good two-phase interface. This structure also provided more storage space for Li_2O_2, which facilitated Li_2O_2 formation/decomposition and contributed to the capacity increase. Among these MCo_2O_4 cathodes, $FeCo_2O_4$ possessed the highest Co^{3+}/Co^{2+} ratio on the surface which was favorable for O_2 adsorption on the active center and showed better electrochemical performance. In addition, Fe^{2+} in the tetrahedral sites easily released electrons to reduce oxygen and was itself oxidized to half-electron filled Fe^{3+}, so that the $FeCo_2O_4$ cathode had a low overpotential. By controlling the nanostructure, the binary metal oxide electrode MCo_2O_4 achieved a lower overpotential and a higher capacity compared to commercial Co_3O_4.

From the above works, it shows that reconciliating the Co^{2+}/Co^{3+} ratio to an optimal value is important for pure Co_3O_4 to exhibit good ORR/OER activity. Strategies reported for optimizing pure Co_3O_4 mainly include the incorporation of noble metals and introducing transition metal components. The noble metals, such as Pd and Ag, often act as a second active site to improve battery performance. The transition metal components can enter the lattice of Co_3O_4 and occupy specific positions to enrich active sites or replace the poorly active low-valent Co to enhance the activity. Meanwhile, the construction of 3D porous network and special micro-configurations is also essential for each improvement strategy. For MnO_2 and Co_3O_4, the modification strategies are more similar, **Table 1** provides the performance statistics of the catalysts with different modification strategies.

Table 1 The comparation of different manganese and cobalt-based catalysts for LABs.

Catalysts	Synthesis method	Electrochemical performance	Catalytic species/ Structural properties	Ref
Sponge-like ε-MnO_2	An oxygen bubble template-assisted electrodeposited way.	5700 mAh g^{-1} at 100 mA g^{-1}; 3400 mAh g^{-1} at 800 mA g^{-1}.	Oxygen vacancies Structural defects Hierarchical porous	80
δ-MnO_2 nano boxes	A controlled stepwise redox reaction method, with Prussian blue analogue as a template.	4368 mAh g^{-1} at 0.08 mA cm^{-2}; 112 cycles with 1000 mA h g^{-1} at 0.16 mA cm^{-2}.	High specific surface area Hierarchical porous	81
Co-salen/ MCNTs@ δ-MnO_2	An ingratiation of the catalyst and the electrolyte approach.	300 cycles with 1000 mAh g^{-1} (0.30 mAh cm^{-2}) at 500 mA g^{-1} (0.15 mA cm^{-2}).	δ-MnO_2 coating layer Mobile O_2-carrier	82
α-MnO_2/ Pd	A typical reduction way, followed by Pd complexation.	261 and 212 mAh g^{-1} after 15 cycles at 0.25 and 1.91 mA cm^{-2}.	Pd complexation Rich mesoporous	86
β-MnO_2/ Au-Pd	A hydrothermal way, with silica KIT-6 as a template.	775 mAh g^{-1} at 0.13 mA cm^{-2}.	Au-Pd complexation Rich mesoporous	87
Pd/bio-MO nanowires	A chemical reaction way with M13 virus as a biological template.	7340 mAh g^{-1} at 0.4 A g^{-1}; 50 cycles with 400 mAh g^{-1} at 0.4 A g^{-1}.	Pd complexation High aspect ratio A porous network	88
α-MnO_2/ Pt/graphene -MWCNTs	A direct reduction and vacuum filtration way.	560 mAh g^{-1} after 10 cycles at 0.01 mA cm^{-2}.	High dispersion Heterogeneous	89
α-MnO_2/ RuO_2	A simple hydrothermal process	50 cycles with 500 mAh g^{-1} at 0.1 mA cm^{-2}.	RuO_2 complexation 3D sea urchin shaped	90
nr-MnO_2/ np-RuO_2	A facile step-by-step hydrothermal method.	500 mAh g^{-1} after 75 cycles at 50 mA g^{-1}; 4000 mA h g^{-1} after 20 cycles at 200 mA g^{-1}.	RuO_2 complexation High dispersion	91
2D IrO_2/δ-MnO_2	A simple two-step	16370 mAh g^{-1} at 200 mA g^{-1}.	RuO_2 complexation Interwoven structure	93

	hydrothermal approach.			
α-MnO_2/ Co_3O_4	A simple two-step hydrothermal approach.	1000 mA h g^{-1} after 60 cycles at 0.1 mA cm^{-2}.	Co_3O_4 complexation Oxygen vacancies	94
CeO_2/δ-MnO_2	A hydrothermal way coupled pH regulation.	296 cycles with 500 mA h g^{-1} at 100 mA g^{-1}.	CeO_2 complexation 3D porous structure	95
3DOS-Co@Mn @CC	A facile step-by-step hydrothermal method.	100 cycles with 500 mA h g^{-1} at 500 mA g^{-1}.	Co_3O_4 complexation 3D open structure	96
Co_3O_4@Ni	A simple chemical deposition reaction.	4000 mAh g^{-1} at 0.02 mA cm^{-2}.	Ni collector 3D network	102
Co_3O_4@Pd	An ingratiation of Pd liquid phase and Co_3O_4 phase way.	5337 mAh g^{-1} after 250 cycles at 100 mA g^{-1}.	Pd liquid complexation	104
Co_3O_4@Co_3O_4/Ag	A facile simultaneous reduction route.	12000 mAh g^{-1} at 200 mA g^{-1}; 4700 mAh g^{-1} at 800 mA g^{-1}.	Ag single atoms/clusters High conductivity Flower-like structure	106
Co_3O_4-e-cPANI	A hydrothermal method coupling with a subsequent calcination.	32478.3 mAh g^{-1} at 100 mA g^{-1}; 226 cycles with 500 mAh g^{-1} at 300 mA g^{-1}.	Hierarchical structure Conductive network	107
$NiCo_2O_4$	A solvothermal method.	6822 mA h g^{-1} at 200 mA g^{-1}; 1000 mA h g^{-1} after 128 cycles at 200 mA g^{-1}	Multilayered core-shell Double-component	110
W-MCO-NWB	A facile hydrothermal method	12919 mAh g^{-1} at 0.1 mA cm^{-2}; 300 cycles with 500 mAh g^{-1} at 0.1 mA cm^{-2}	Interconnected porous Double-component	111

3.3 Other transition metal compounds

TiC has been widely explored as a potential electrode for LAB due to several attractive

characteristics[113-115] such as the excellent conductivity, low side reactions during electrocatalysis, and favorable formation and decomposition of Li_2O_2.

Ottakam Thotiyl et al.[116] developed a series of LAB cathode catalysts (TiC, TiN, and SiC) and tested on LAB of the corresponding electrodes using two electrolytes, dimethyl sulfoxide (DMSO), and tetraethylene glycol dimethyl ether (TEGDME). Since the cell polarization in the reaction increased with the number of TEGDME electrolyte cycles, the cell capacity retention of DMSO was higher than that of TEGDME. In addition, x-ray photoelectron spectroscopy (XPS) characterization of the electrode surfaces after charge-discharge cycles detected a large amount of TiO_2 and TiOC on the TiC electrode surface after cycling. In comparison, the SiC showed no oxide layer, and while TiN exhibited an oxide, the conductivity was lower compared to the TiC. Thus, the TiC electrode exhibited the most stable and high conductivity attributed to the formation of thin passivated surface layers of TiO_2 and TiOC, which ensured reversible Li_2O_2 formation/decomposition, i.e., after 100 cycles, almost 99.5% of the product was Li_2O_2 and the capacity retention was more than 98%.

Further studies found that when the surface oxide layer (TiC/TiOC/TiO_2) of the TiC electrode reaches 2-3 nm thick, the electron transfer during electrocatalytic reaction will be sufficiently inhibited, which is detrimental to the charging overpotential and LAB performance of the cell.[117, 118] Based on this, once the thin oxide layer is formed, the LAB with the TiC electrode exhibits high stability during cycling.

Further research on the effect of nano passivation on LAB cathodes was reported by Adams et al.[119] In this study, TiC powders were prepared by selecting TiC-A and TiC-B from different suppliers, and TiN was selected for comparison and used as electrode materials for

electrocatalytic performance testing. The results showed that the two TiC powders had similar bulk properties but different surface properties. The surfaces of the powder materials were examined by XPS and scanning transmission electron microscopy (STEM), and it was observed that TiC-A had an amorphous layer (thickness of about 2-3 nm) on the surface. The structure was sufficient to prevent electron transfer, and this prevented charging (i.e., did not support OER). In contrast, the TiC-B particles were not surrounded by an amorphous layer and thus charging of Li_2O_2 was possible.

Jeong et al.[120] prepared a vertically aligned TiC-coated carbon cloth (TiC-cloth) by growing TiC on the surface of cotton T-shirts (carbon cloth 10 × 10 cm^2) through a simple carbothermal process and used it as a LAB cathode. On the one hand, the vertically aligned TiC-cloth protected the carbon surface, i.e., inhibited carbon decomposition. On the other hand, this special structure offered sufficient surface area for the Li_2O_2 discharge product, which ensured that Li_2O_2 grew along the shape of TiC and could undergo reversible formation and decomposition **(Fig 9(a))**. As a result, electrochemical testing showed that the TiC-cloth had a higher capacity **(Fig 9(b, c))** and superior cycling stability **(Fig 9(d))** compared with TiC nanoparticle electrodes cast on T-shirts.

Given that transition metal nitride cathodes are cheaper than noble metals, titanium nitride (TiN) is considered as a promising cathode material for LAB.[121, 122] However, TiN can only catalyze oxygen reduction (ORR) and cannot promote the oxidation of Li_2O_2 (OER), which hinders its practical application in LAB. The reason for this significant drawback of TiN is that when Li_2O_2 is present, the TiN surface will be oxidized and the charge transfer resistance increase dramatically, thus inhibiting oxygen precipitation.[123-125]

To overcome these drawbacks, Kim et al.[122] synthesized a mesoporous titanium nitride (m-TiN) catalyst with a 2D hexagonal structure using a block copolymer template and evaluated this material as an air cathode skeleton in LAB. The synthesized m-TiN had a good pore structure and good electrical conductivity, which made the cell reaction fully reversible, resulting in good cycling performance for more than 100 cycles. In addition, the introduction of a nonporous polyurethane separator protected the Li metal anode, further ensuring that the LAB maintains an initial capacity of 280 cycles at 430 mAh g^{-1}.

A 3D array catalyst material (TiN@Pt_3Cu) of Pt_3Cu alloy particles (10 wt%, diameter ≈ 2-5 nm) uniformly decorated with special flower-like 1D highly oriented crystalline TiN nanowires (diameter ≈ 100 nm) was synthesized by Luo et al.[126] and used as a porous air electrode for LAB **(Fig 9(e)).** The 1D, highly oriented TiN nanowire arrays were applied as air electrode frameworks and alloy catalyst carriers to create a high conductivity network, exhibiting better electrochemical stability than carbon. In addition, the uniformly deposited icosahedral Pt_3Cu nanocrystals with abundant (111) active crystal planes and multiple twin boundaries imparted a high catalytic activity. The high conductivity TiN@Pt_3Cu network structure had promoted the rapid diffusion and catalytic reaction of gas and electrolyte during cycling. The battery was subjected to 50 cycles at 0.2 mA cm^{-2} in 1000 mAh g^{-1} capacity-limited mode, and the results showed a terminal discharge voltage greater than 2.7 V and a charging voltage less than 3.73 V exhibiting good reversibility **(Fig 9(f))**.

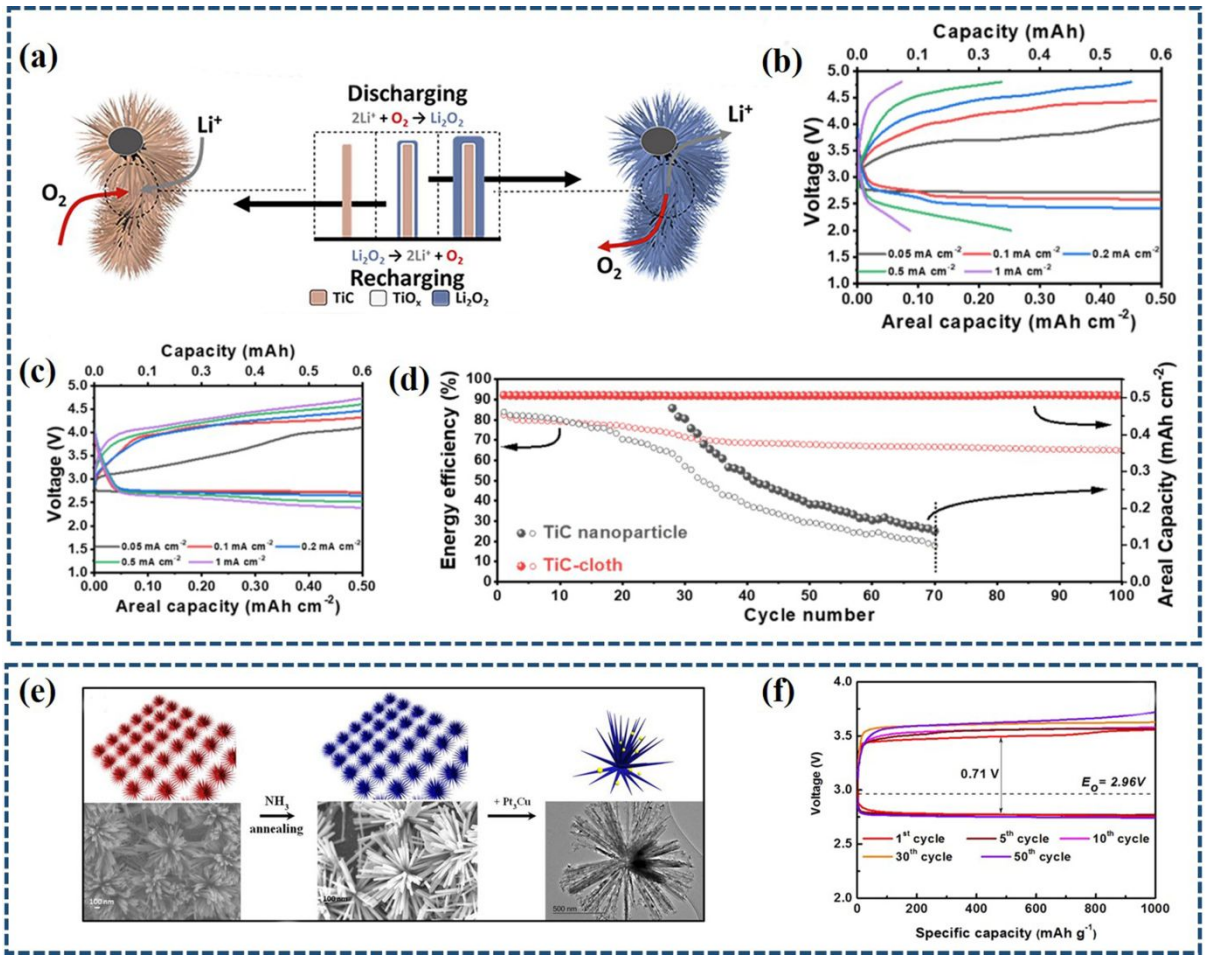

Figure 9 (a) Schematic diagram of discharging/recharging LAB using a TiC-cloth cathode; Discharge-charge distribution measured at different current densities under a capacity limit of 0.5 mAh cm^{-2} of **(b)** TiC NPs and **(c)** TiC-cloth cathode; **(d)** The cycle performance graph of energy efficiency at certain areal capacity;[120] Copyright 2020 Elsevier. B.V. **(e)** Schematic diagram of the formation of TiN@Pt_3Cu air electrode and SEM image; **(f)** Discharge and charging curves for selected cycles of TiN@Pt_3Cu composites.[126] Copyright 2017 American Chemical Society.

Apart from carbides and nitrides, transition metal sulfides also have been regarded as the promising bifunctional catalysts for LAB[39], such as, flower-like NiS,[127] 2D Co_3S_4 nanosheets, [128] 3D foam-like porous Ni_3S_2,[129] flower- and carambola-like CuS,[130] and so on. Prominently, MoS_2 showed attractive application prospects, but still faces the problems of low

conductivity and poor stability. In view of the above, Hu et al,[131] synthesize 3D interconnected network MoS_2/CNTs catalysts by integrating carbon nanotubes on ultrathin MoS_2 nanosheets via a one-step hydrothermal way **(Fig 10(a))**. The highly dispersed CNTs improved conductivity and the interconnected architecture boosted rapid mass transfer, both synergistically overcoming the drawbacks of pure MoS_2. The LAB based on MoS_2/CNTs realized an excellent discharge capacity of 6904 mA h g^{-1} at 200 mA g^{-1}, which was higher than that of pure MoS_2 (6117 mA h g^{-1}) **(Fig 10(b))**. Some transition metal sulfides have a specific pro-oxidant nature and are also of interest to researchers. Lin et al.[132] prepared Co_9S_8-PCF catalysts for LAB with needle-like Co_9S_8 nanorods grown on porous carbon foils, which possessed the 3D sisal and open structure. Benefiting from the oxygen-affinity nature of Co_9S_8 nanorods, Li_2O_2 particles were uniformly deposited on their periphery, forming a flower-bud-bunch Li_2O_2/cathode contact interface. The 3D sisal structure of Co_9S_8-PCF ensured sufficient storage space for Li_2O_2 deposition, and its open structure reduced the resistance to oxygen release, making Li_2O_2 easier to decompose. These realized a high 6875 mA h g^{-1}discharge capacity at 50 mA g^{-1} and a low 0.57 V overpotential under 1000 mA h g^{-1}.

Transition metals sulfides supported on heteroatom-doped carbon materials have been used as efficient bifunctional catalysts in several studies, such as, FeS-C (N/S-doping),[133] CoS NWs@NSC (N/S-doping),[134] Co_9S_8/C (N-doping),[135] and so on. However, the simple mixing of the two makes them insufficiently contactable and prone to separation, which affects the electron transfer rate and shortens the life of the battery. Therefore, Cao et al.[136] adopted an electrospinning and post-high-temperature calcination approach to fabricate N/S-doped porous carbon nanofiber-supported Co_9S_8 nanoparticle (graphitic shell-encased)

catalyst (Co_9S_8@G/NS-PCNF) for LAB **(Fig 10(c))**. Special N/S doped carbon frames effectively synergized with uniformly distributed Co_9S_8 nanoparticles to catalyze ORR and OER, without any flaking whatsoever. Finally, the discharge capacity is up to 8269 mAh g^{-1} (@100 mA g^{-1}) with a polarization gap as small as 1.52 V **(Fig 10(d))**.

Considering the easily tunable electronic structure of transition metal sulfides, many studies have focused on replacing the central transition metal cation with other cations to achieve its structural tuning and to improve the catalytic performance. Recently, Cu-doped CoS_2 nanoparticles bifunctional catalysts (Cu-CoS_2) for LAB are fabricated by Ding et al. [137] through a solvothermal method. Few electrons were transferred from Co to O (Li-O) because the introduced Cu facilitated the transfer of electrons from Co to S in the Co-S covalent bond **(Fig 10(e))**. This leaded to weakened adsorption of Li-O intermediates on the Cu-CoS_2 surface, further improving the reversibility and cycle life of the LAB **(Fig 10(f))**.

Not only the two-component catalysts of transition metal oxides mentioned above have attracted much attention, but also binary transition metal sulfides as efficient bifunctional catalysts.[138, 139] The ease of tunability of their electronic structure also supports the development of their two-component catalysts. Particularly, Ni/Co sulfides stands out for having excellent characteristics of high conductivity and an abundance of active sites provided by the two metal ions.[140, 141] Recently, a yolk-shell $NiCo_2S_4$ catalysts for LAB was obtained by Xu et al. [142] via a simple two-step hydrothermal approach. The typical synergistic effect from Ni and Co ions were present in $NiCo_2S_4$ for ORR and OER catalyzation. Additionally, the special yolk-shell structure with a largest gap contributed to enhanced

catalytic kinetics, coupled with high-activity (531) lattice plane, further manifesting in a high capacity and an optimal rate capability of the LAB. That is, the induction of special structures and high-index crystalline surfaces is essential to enhance the catalytic performance of binary transition metal sulfide catalysts. Further integration with carbon materials is also one of its future directions. [143]

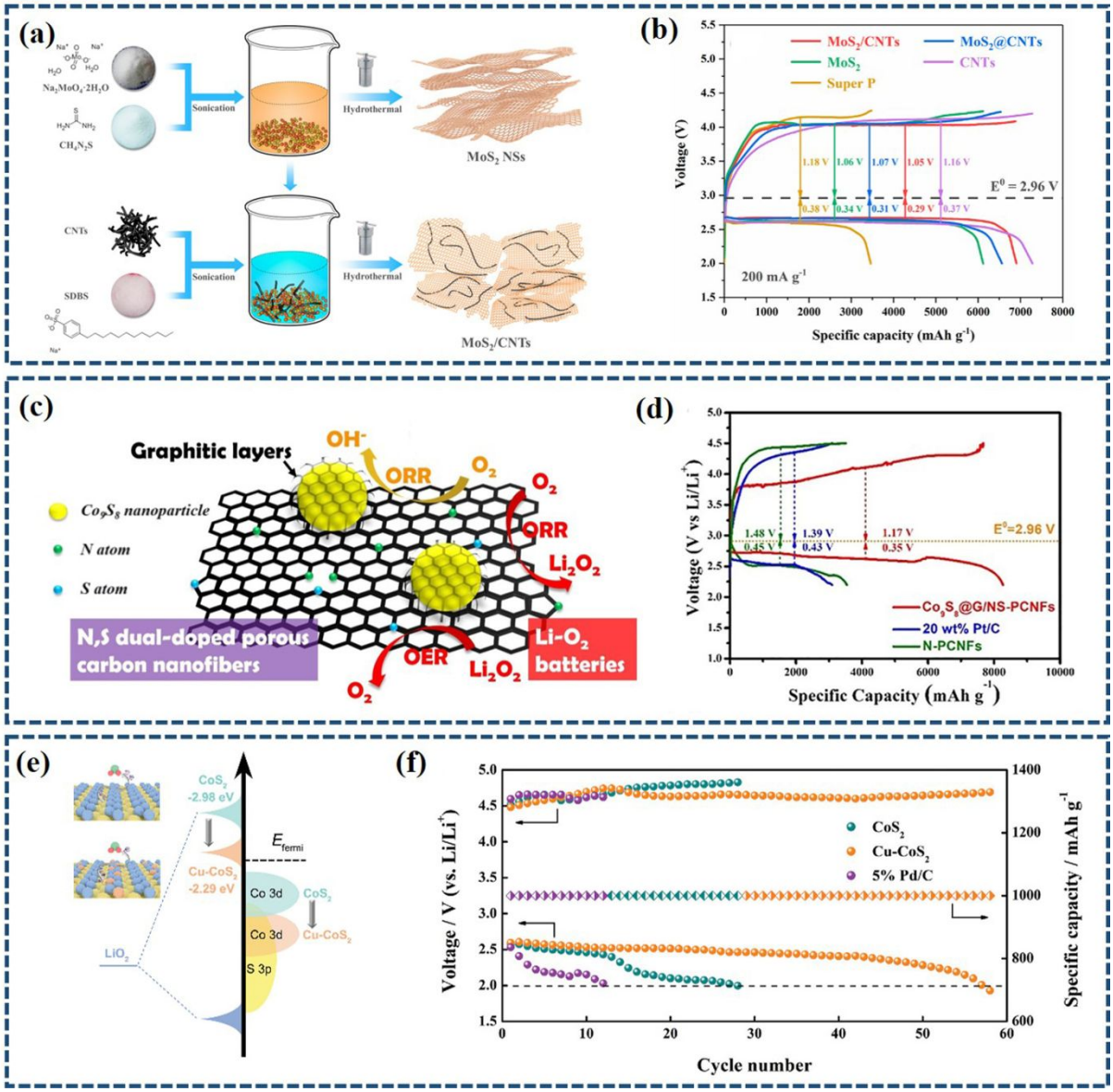

Figure 10 (a) Schematic map of the preparation of MoS_2/CNTs; **(b)** The discharge-charge curves of

MoS_2/CNTs based LAB at 200 mA g^{-1}. Copyright 2018 American Chemical Society.[131] **(c)** Sketch map of Co_9S_8@G/NS-PCNFs structure. **(d)** The first discharge-charge curves of LAB with Co_9S_8@G/NS-PCNFs as cathode catalysts at 100 mA g^{-1}. Copyright 2019 Elsevier B.V. [136] **(e)** Schematic diagram for the reformative performance of CoS_2 after Cu doping. THE cycling performance of Cu-CoS_2 for LAB at 600 mA g^{-1}. Copyright 2023 Wiley-VCH GmbH. [137]

To summary, for TiC, the formation of a thin oxide layer is beneficial to maintain high electrical conductivity to ensure the formation/decomposition of Li_2O_2. Conversely, the formation of an amorphous layer on its surface is not conducive to electron transfer, thus reducing the catalytic activity. For the more economical TiN, constructing a good pore structure and loading alloy nanoparticles are important strategies to overcome its susceptibility to oxidation during the OER process, thus further promoting its bifunctional catalytic applications. For transition metal sulfides with relatively poor electrical conductivity, complexation with carbon materials is a typical strategy for optimizing their catalytic properties. Based on the easy adjustment of their electronic structure, the substitution of central metal ions and the development of two-component catalysts are also in the trend of their development.

3.4 Carbon materials

The performance enhancement strategies for several types of catalysts discussed in the above sections inevitably involve compounding with carbon materials. This is due to the superior conductivity and high specific surface area of carbon materials, which are always used as conductive additives or carriers. The low-cost and eco-friendly carbon materials can

not only be used as an auxiliary part to enhance the activity of the catalyst, but can also be used directly as efficient catalysts after appropriate modification.

The most practicable and effective method is to perform doping modification to prepare carbon-based catalysts for LAB. N-doped carbon catalysts were shown to have prominent bifunctional catalytic potential.[144, 145] In early stage， Mi et al.[146] adopted a special floating catalyst chemical vapor deposition approach to grow N-doped carbon nanotubes catalysts (N-CNT) on nickel foam for LAB. With the increase of N content, the discharge products were uniformly distributed on the N-CNT surface and completely decomposed during the charging process, further exhibiting excellent cycling performance. This proves that uniform distribution of the discharge products plays an important role in the manifestation of high catalytic activity.

Notably, their morphology is also an important determinant of the catalytic activity, which can be adjusted by N doping. For this perspective, Lyu et al. [147] used stepwise pyrolysis of basic magnesium carbonate precursor and pyridine to obtain hierarchical N-doped carbon nanocages catalyst (hNCNC) for LAB, assisted by MgO template. Benefiting from the enhanced O_2 adsorption due to N doping **(Fig 11(a))** and the high specific surface area ensured by the carbon nanocages, the Li_2O_2 grew into large thin film not into typical toroid on the hNCNC surface **(Fig 11(b))**. This contributes to the simultaneous realization of a high discharge capacity (9.1 mAh cm^{-2} @ 0.05 mA cm^{-2}) and a low charge overpotential (4.2 V) **(Fig 11(c))**. In analogous to N, the introduction of other heteroatoms (e.g., B, P, Cl, etc.)[148-150] into carbon can also modulate its crystal lattice, induce the charge redistribution,

and optimize the surface adsorption properties. For S with little difference in electronegativity, it can polarize the molecular orbitals, thus shortening the band gap and facilitating the surface adsorption.[151]

In addition to increasing the bifunctional catalytic activity of the catalyst, attention should be paid to the improvement of its stability. Especially, for OER, it occurs at a high potential, which can cause severe corrosion of carbon materials. To overcome this problem, Yang et al.[152] prepared an N-Co-O triple-doped carbon catalyst by pyrolyzing polyaniline, cyanamide, and cobalt salts in an N_2 atmosphere. Notably, the better contact of molten cobalt chloride with the carbon phase facilitated to form a more homogeneous and efficient Co dopi000ng compared to solid cobalt oxide **(Fig 11(d))**. The uniformly dispersed Co favored the formation of N-Co-O triple-doped carbon and Co-O species, which interacted with graphitized-N to produce high OER activity. This works proves multiple doping can overcome some of the disadvantages that are insurmountable with single doping. The synergistic interaction between multiple dopants can lead to larger charge redistribution and induce more active sites, which is a more promising research direction for efficient carbon-based catalysts. So for, a series of multiple doping carbon-based catalysts have been developed with extraordinary bifunctional catalytic potentials, such as, N/S co-doping graphene nanosheets,[153] N/P/F-doped graphene,[154] B/N-doped graphene,[155] thiophene-S-doped graphene,[156] N/P co-doping graphene-like carbon nanosheets,[157] and so on.

The construction of hierarchical porous structure for carbon-based catalysts is another effective method to optimize their catalytic properties. In early stage, Guo et al.[158] prepared

3D carbon sphere array catalysts with ordered mesoporous channels and hierarchical meso-/meso-porous structures (i.e., MMCSAs) **(Fig 11(e))** for LAB utilizing a macro-porous silica skeleton (calcined from templated silica alkoxy precursors around polystyrene spheres) as a template. The special pore structure of MMCSAs favored electrolyte penetration and ion diffusion and supplied a space for the conversion of O_2/Li_2O_2 **(Fig 11(f))**, which resulted in a stable discharge curve with a discharge voltage of about 2.5 V even at 1000 mA g $^{-1}$**(Fig 11(g))**.

On the other hand, the side products on the carbon-based catalyst surface can be restrained by adjusting their pore structure. Lim et al.[159] developed 3D graphene hollow sphere bifunctional catalysts (CB-H) for LAB via the hydrocracking of vacuum residue with the auxiliary effect of Fe_3O_4 at supercritical environment. The tailored bubble-like multi-layered pore structure only afforded a storage space for Li_2O_2, so that the production of by-products was effectively suppressed. The green and low-cost CB-H catalyst promoted a higher discharge capacity of 18578 mA h g^{-1} at 50 mA g^{-1} than other reported commercial carbon. To this day, this modification strategy is revered and explored by most for developing efficient bifunctional carbon-based catalysts , such as, P-doped hive-like porous carbon, [160] sawdust-derived porous carbon, [161] edge-rich N doping porous carbon, [162] and so on.

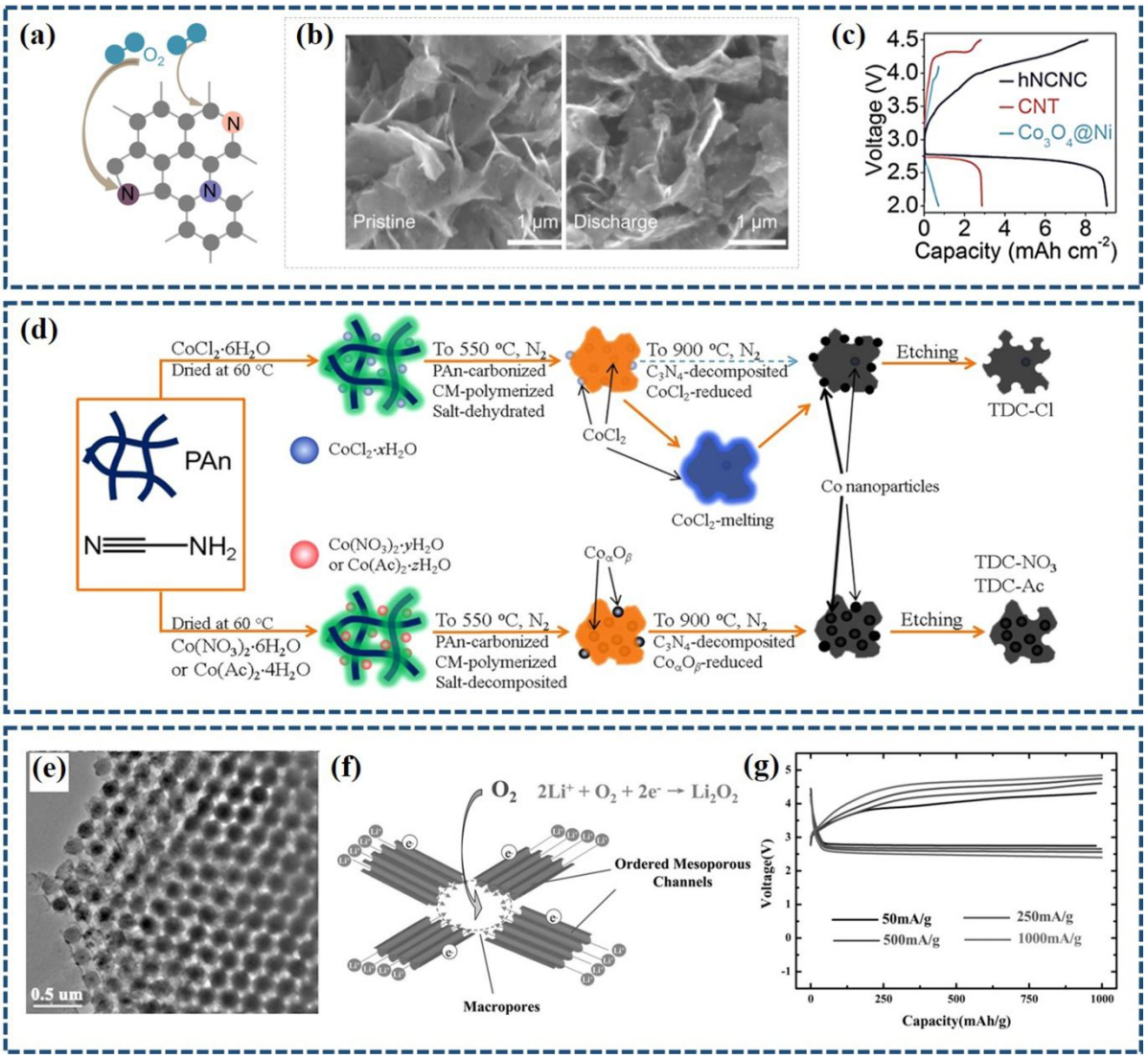

Figure 11. **(a)** Schematic map of enhanced O_2 absorbability on hNCNC; **(b)** SEM images of hNCNC before and after discharging. **(c)** First discharge-charge curves of hNCNC at 0.05 mA cm^{-2}. Copyright 2017 Elsevier Ltd.[147] **(d)** The reaction schematic diagram of precursors with different cobalt salts. Copyright 2016 American Chemical Society.[152] **(e)** TEM image of MMCSAs; **(f)** Sketch map of the conversion of O_2/Li_2O_2 in MMCSAs; **(g)** Discharge/charge curves of MMCSAs (30 wt%) for LAB with 1000 mAh g^{-1} at a series of current densities. Copyright 2013 WILEY-VCH Verlag GmbH & Co. KGaA, Weinheim.[158]

Therefore, carbon materials have the advantages of high electrical conductivity, large

specific surface area, easy doping, and easy perforation. The first two intrinsic properties favor them as adjuvants. The latter two essential properties facilitate their structural modification and thus enhance their bifunctional catalytic performance. There are more defects after heteroatom doping, which can provide reactive sites to enhance the catalytic activity. The mesopores are helpful for mass transfer and the macropores can offer enough discharge product storing space, further accelerating reaction kinetics, and improving stability. Despite the obvious advantages of carbon-based bifunctional catalysts, they still face long-term stability issues, thus, the study of other catalysts remains essential.

4. Other essential components of LAB

In addition to cathode material selection, it is equally important to consider other components of LAB such as the Li metal, electrolyte, and separator. These components significantly affect the performance of the cell in practical applications. [163] To achieve efficient ORR and OER performance, a comprehensive understanding of the factors affecting these components is necessary.

Li metal anodes (LMA) have attracted great attention owing to their huge theoretical capacity (3860 mAh g^{-1}), low gravimetric density (0.534 g cm^{-3}), and low redox potential (-3.04 V vs standard hydrogen electrode). Thus, LMA are regarded as the most promising anode for LAB and can deliver a high theoretical specific energy of 11700 Wh kg^{-1}. [164, 165] However, there are still many unsolved problems that limit their deployment such as infinite volume expansion during charging/discharge, its hyperactive nature, irreversible Li deposition (i.e., formation of dead Li), and Li dendrite formation resulting in short-circuit [166-

[168]. These problems reduced capacity retention during cycling and compromised battery safety. The highly reactive Li metal may be eroded by electrolyte solvents and additives causing a series of side reactions that reduce the efficiency of the Li anode.

To address the problem of Li dendrites in LAB systems, promising strategies have been proposed, such as Li metal surface passivation (physical or chemical methods)[169-171], the use of solid-state electrolytes [172], and the development of Li lithophilic nanostructured Li hosts[173]. Additional strategies include engineering an electrolyte-additive-based solid electrolyte interphase (SEI), [174, 175] solid polymer composite electrolytes, [176] and separator surface modification. [177, 178] The addition of a protective "hard film" layer can prevent direct contact between the Li and other components, which in turn inhibits side reactions and suppresses Li dendrite growth. Xu et al.[179] prepared a stable tissue-directed/reinforced bifunctional separator/protection film (TBF) for LAB, which can help to prolong the battery life for 300 cycles. Yan et al.[180] reported a hydrophobic hybrid polymer electrolyte film for protecting Li metal anodes which exhibited high stability, hydrophobicity, and flexibility. Zhang et al.[181] reported that the addition of 1,4-dioxanylcyclohexane to the electrolyte could form an SEI film on the Li metal surface, and this LAB with protected Li anode could achieve a cycle life of 60 cycles even if conventional KB was used for the air cathode.

Li thiophilic nanostructured composite anodes can guide uniform Li plating/stripping mechanism. [182] For instance, Chi et al.[183] prepared a Li/Ni composite anode by placing a nickel foam disk on top of molten Li and incorporated this anode into a symmetric cell that exhibited a cycle stability of 2400 h. Analysis of the Li stripping/plating behavior revealed that the nickel foam acted as a stable host for preexisting Li and could accommodate the

anode surface energy during electrochemical cycling, thus preventing the growth of Li dendrites and limiting the Li electrode expansion to ≈3.1% **(Fig 12)**.

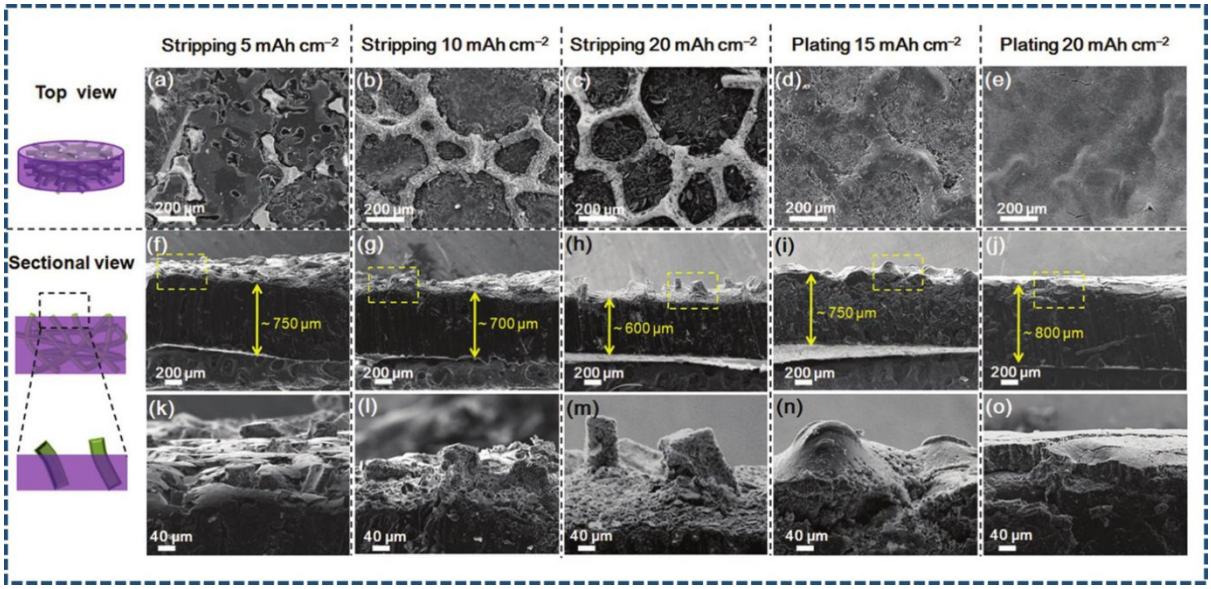

Figure 12 Surface and cross-sectional SEM graphics of the Li/Ni composite with a Li stripping of **(a, f, k)** 5 mAh cm^{-2}, **(b, g, l)** 10 mAh cm^{-2}, and **(c, h, m)** 20 mAh cm^{-2}; then plating of **(d, i, n)** 15 mAh cm^{-2} and **(e, j, o)** 20 mAh cm^{-2} at 1 mA cm^{-2}.[183] Copyright 2017 WILEY-VCH Verbg GmbH&Co. KGaA, Weinheim.

Non-aqueous electrolytes include non-protonic electrolytes and solid electrolytes. So far, studies on non-protonic electrolytes have shown that they are susceptible to decomposition, volatility, low electrical conductivity, low oxygen solubility, high sender number, and high viscosity, and that they are prone to frequent side reactions with Li anodes, oxygen, and intermediate species, thus limiting their marketable applications.[184, 185] On the contrary, solid-state electrolytes (SSEs), are not prone to volatilization and leakage and their ability to effectively inhibit Li dendrite growth and resist corrosion by oxygen-containing species shows great promise for market applications.[186, 187]

For example, Zhang et al. [188-190] developed a series of SSEs for LAB, including

NASICON-type, garnet-type, PEO-type, and hybrid materials (e.g., $Li_7La_3Zr_2O_{12}$ (LLZO)). In addition, a series of polymer electrolytes were systematically summarized and highlighted that polymer electrolytes were more suitable than ceramic electrolytes as an alternative to liquid electrolytes because of their excellent processing properties and mechanical strength.

Although some progress has been made in solid-state electrolytes, some thorny issues remain such as low electrical conductivity and poor electrode contact. With this in mind, "quasi-solid" polymer electrolytes (QSPEs) have been proposed by researchers as a transition option. For example, Wu et al.[191] made a superhydrophobic and waterproof quasi-solid electrolyte (SHQSE) **(Fig 13(a))** using a nonwoven fabric as a porous substrate, a mixture of silicon dioxide (SiO_2, superhydrophobic) and polyisobutylene (PIB, binder) in heptane as the coating, and 100°C under vacuum for the drying. This novel quasi-solid electrolyte with high ionic conductivity and super-hydrophobicity showed a long cycle life and excellent safety when operating in LAB at 45% relative humidity (RH) **(Fig 13(b, c))**.

Recently, Kondori et al.[192] used a silane coupling agent to couple the Li-rich $Li_{10}GeP_2S_{12}$ NPs with a modified polyethylene oxide polymer carrier to create a novel composite polymer electrolyte for room-temperature-LABs. In situ Raman spectroscopy measurements of the products proved that the catalytic reaction proceeded along the 4*e* pathway with Li_2O as the main product **(Fig 13(d))**. This result confirmed in the titration experiments combined with UV-Vis spectroscopy. These SSE in LAB yielded a stable operation for 1000 cycles and exhibited a small polarization gap **(Fig 13(e, f))**.

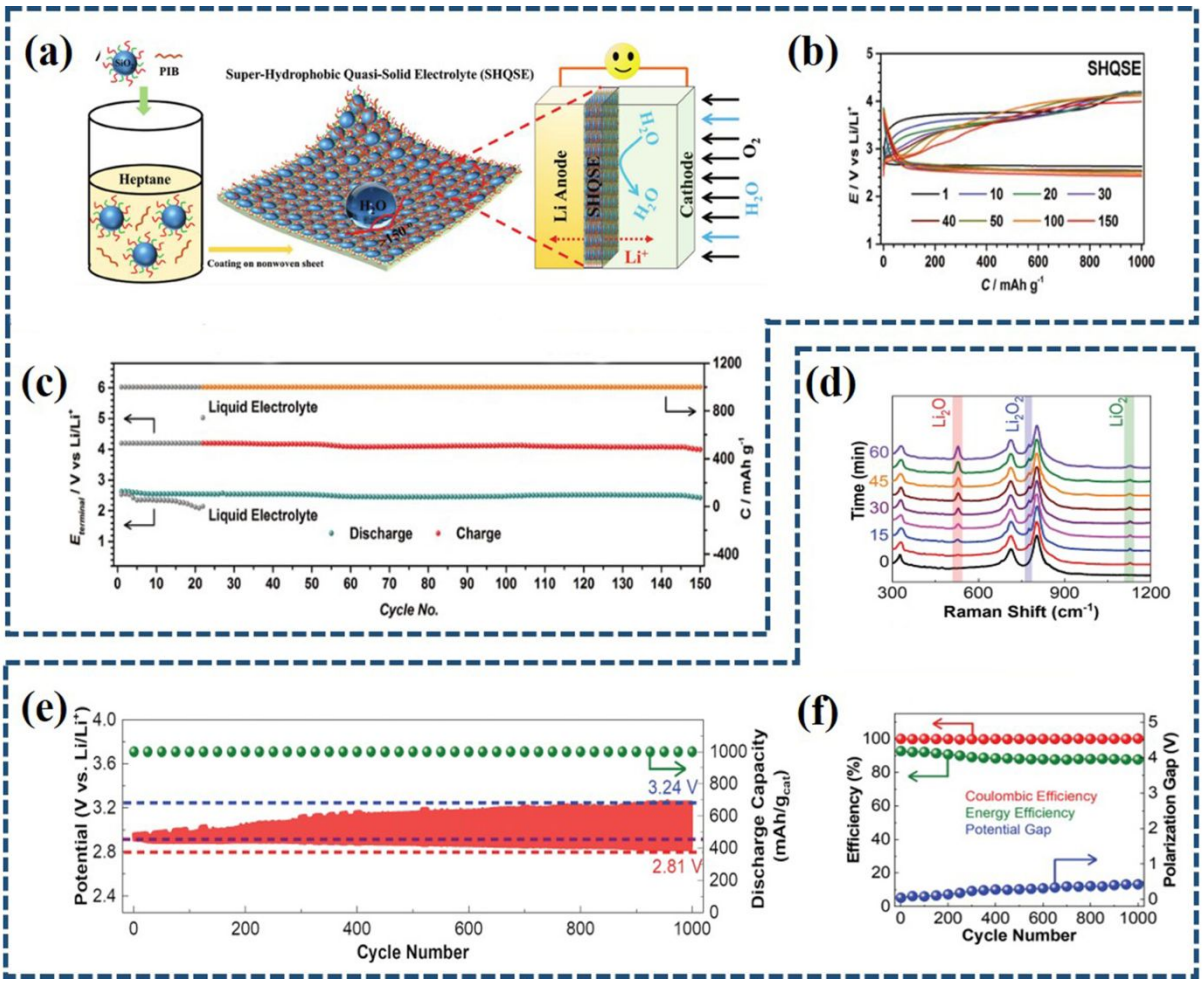

Figure 13 (a) Schematic diagram of a solid-state LAB based on super sparse level solid electrolyte (SHQSE) in a humid atmosphere; Typical charge and discharge curves of LAB at RH of 45%: **(b)** SHQSE, **(c)** Discharge and charge end voltages and discharge capacity versus cycle number (Current density:500mA g^{-1}).[193] Copyright 2017 WILEY-VCH Verbg GmbH&Co. KGaA, Weinheim. **(d)** In situ Raman spectroscopy for monitoring the products during ORR at 1 A/g with $Li_{10}GeP_2S_{12}$ coupled SSE in the LAB; **(e)** Constant current cycle over 1000 cycles of battery performance; **(f)** The coulombic/energy efficiency, and polarization gap over 1000 cycles at 1 A/g and under 1 Ah/g.[192] Copyright 2023 Science.

In addition to the primary components mentioned above, the LAB (air environment) still needs a selective membrane for screening the gas (O_2/CO_2) to block moisture and for

preventing the transport of electrons and reactive oxygen species between the cathode and the anode.[194-196] Depending on the requirement, this selective membrane should have a suitable pore structure, which in turn allows O_2 transport. Recently, Xie et al.[197] synthesized an oxygen-permeable waterproof membrane based on perfluoropolyether (PFPE). PFPE is a non-volatile, highly hydrophobic liquid polymer that is selectively permeable to non-polar O_2 molecules and its chain mobility facilitates O_2 diffusion. As a result, the stability of both Li metal and Li peroxide in the reaction was markedly enhanced under the protection of the PFPE-wetted Celgard film, enabling the LAB to run for 144 cycles (~58 days) in 30% relative humidity in air. Of course, solid electrolytes can also be useful as separators, for example. Lee et al.[198] prepared an ultrathin film by depositing ion-conducting polymers and graphene oxide on a polymer support film by layer-by-layer self-assembly. This special process was accomplished by hydrogen bonding between poly (ethylene oxide) (PEO), facilitating Li transport, and a nanoscale selective barrier layer, GO, while poly (acrylic acid) (PAA), acting as an intermediate layer, also forms hydrogen bonds with PEO. The membrane had a controlled electrolyte permeability (1.42×10^{-12} m^2), a high ionic conductivity (0.29 mS cm^{-1}), and a high Li transfer number (0.52); at the same time, the membrane successfully prevented Li dendrite growth and improved the recyclability of the Li anode up to 281.1 h.

5. Conclusion and outlook

In conclusion, the development of a new generation of green lithium-air batteries (LABs) to meet the growing demand for energy storage technology is an important contribution to promote the sustainable development of contemporary society. Specifically, to overcome the

low-round trip efficiency, poor cycling stability and rate capability, and insufficient practical energy density for LABs, a fundamental understanding of ORR and OER mechanisms of LABs is essential. It is also necessary to achieve a deep understanding of advanced cell design principles, nanoscale material synthesis, and the synergic effects of cathode structures and the above mentioned bifunctional electrocatalysts on LAB performance. A roadmap for future development can be described as follows:

First, an in-depth understanding of the ORR and OER mechanisms underlying LAB operation is essential for the construction of high specific capacity and long cycle life battery systems. Exploring the detailed role of catalyst active sites at the electrochemical interface can contribute to the rational design and development of highly active and selective functional catalyst materials for LABs. In addition, understanding the formation and decomposition mechanisms of discharge products, intermediate phase by-products, and the nucleation mechanisms of Li anodes will contribute to the improvement of LABs stability. Advanced in situ characterization techniques to directly observe the structural evolution of electrodes and qualitatively probe the physical phase of intermediates can provide a detailed picture of the interfacial reactions, and inform the design and optimization of key components of LABs. In addition, theoretical models, and simulations to calculate parameters such as energy band centers, bond energy, and adsorption energy, will create a detailed understanding of the complex electrochemical reactions in LAB and guide the development of novel materials.

Next, the development of high-activity and high-capacity air cathode materials is the key to achieving high-performance LABs. This review focused on the research progress of

nanoscale bifunctional catalysts, as well as the design and analysis principle of corresponding materials and the special cathode structure towards high-performance LABs. The synthesis of high-efficiency air cathode catalysts should follow certain guidelines: (1) adjust the crystal structure, morphology, and size to achieve highly active crystalline phases; (2) create 3D porous networks to provide sufficient storage space for discharge products, and provide multiple phases for e^- O_2, Li^+; (3) construct layered structural systems or adjustable multilayer structural systems to increase the contact area between Li_2O_2, electrolyte, and electrode; (4) introduce defects and other active phases, especially, coupling various active catalysts to improve the catalytic activity of ORR and OER. Accordingly, materials with heterogeneous structures which show higher discharge/charge capacity and cycle life due to the coupling with adjacent characteristics and controlled ORR/OER active phases, are a promising class of highly efficient cathode materials for LABs, which will also be the trend in the design and development of highly efficient cathode materials for LABs.

Plus, to build practical LABs, key components such as the Li anode, electrolyte, and separator should be designed and optimized rationally. Modification of the Li anode is needed, such as the formation of an artificially protected SEI film interface by physically or chemically covering its surface with protective materials or the careful design of its structure, which in turn inhibits the growth of Li dendrites. Lastly, there is a need to develop high ionic conductivity solid electrolytes or highly selective separators to block airborne contaminants and purify the reaction.

Moreover, the precise structural design of catalysts capable of modulating the reaction pathway will become increasingly important to achieve high LABs efficiencies. It will appear

to be important to gain an in-depth understanding of the side reactions during ORR and OER by adopting advanced in situ monitoring techniques. The analyses of full cell level to evaluate the LAB performance will be essential, and the optimization strategies should focus on this level or even larger package level. The optimal market of the LABs should be examined and it is necessary to bring this technology to market as quickly as possible. These problems needed to be overcome by the collaborations of scholars from various fields.

Conflicts of interest

The authors declare no competing interest.

Author contributions statement

Jinyu Zhao: Conceptualization; Methodology; Data Curation; Writing-original draft; Writing-review & editing.

Rajesh Pathak: Methodology; Writing-review & editing; Validation; Grammatical revision.

Zhenxin Zhao: Writing-review & editing; Grammatical revision.

Xu Chen: Writing-review & editing; Validation.

Hansheng Li: Writing-review & editing; Grammatical revision.

Madan Bahadur Saud: Validation; Grammatical revision.

Fan Wu: Writing-review & editing; Grammatical revision.

Quinn Qiao: Validation; Supervision.

Jeffrey W Elam: Validation; Supervision.

Xiaomin Wang: Resources; Funding acquisition; Supervision.

Acknowledgments

This work has been supported by the National Natural Science Foundation of China (52072256), Shanxi Science and Technology Major Project (20201101016), Key R&D program of Shanxi Province (202102030201006, 202202070301016), Central guide local science and technology development funding program (YDZJSX2021B005). Science and technology innovation base construction project of Shanxi Province (YDZJSX2022B003). R. Pathak acknowledges financial support from Laboratory Directed Research and Development (LDRD) funding from Argonne National Laboratory. M. Saud and H. Li acknowledge the support from NSF IUCRC Center for Solid-State Electric Power Storage (CEPS).

References

1. M. Athika, V. S. Devi and P. Elumalai, *ChemistrySelect*, 2020, **5**, 3529-3538.
2. H. Wang, X. Wang, M. Li, L. Zheng, D. Guan, X. Huang, J. Xu and J. Yu, *Advanced Materials*, 2020, **32**, 2002559.
3. J. Zhao, J. Lian, Z. Zhao, X. Wang and J. Zhang, *Nanomicro Lett*, 2022, **15**, 19.
4. M. S. Whittingham, *Science*, 1976, **192**, 1126-1127.
5. K. M. Abraham and Z. Jiang, *Journal of The Electrochemical Society*, 1996, **143**, 1.
6. J. Read, *Journal of The Electrochemical Society*, 2002, **149**, A1190.
7. T. Ogasawara, A. Débart, M. Holzapfel, P. Novák and P. G. Bruce, *Journal of the American Chemical Society*, 2006, **128**, 1390-1393.
8. W. J. Kwak, Rosy, D. Sharon, C. Xia, H. Kim, L. R. Johnson, P. G. Bruce, L. F. Nazar, Y. K. Sun, A. A. Frimer, M. Noked, S. A. Freunberger and D. Aurbach, *Chem Rev*, 2020, **120**, 6626-6683.
9. C. Shu, J. Wang, J. Long, H.-K. Liu and S.-X. Dou, *Advanced Materials*, 2019, **31**, 1804587.
10. A. I. Belova, D. G. Kwabi, L. V. Yashina, Y. Shao-Horn and D. M. Itkis, *The Journal of Physical Chemistry C*, 2017, **121**, 1569-1577.
11. J. Huang and A. Faghri, *Journal of Power Sources*, 2016, **307**, 45-55.
12. V. Pande and V. Viswanathan, *ACS Energy Letters*, 2016, **2**, 60-63.
13. Z. Liang and Y.-C. Lu, 2021, **4**, 1588-1598.
14. W. Zuo, M. Luo, X. Liu, J. Wu, H. Liu, J. Li, M. Winter, R. Fu, W. Yang and Y. Yang, *Energy & Environmental Science*, 2020, **13**, 4450-4497.
15. M. Wang, Y. Yao, X. Bi, T. Zhao, G. Zhang, F. Wu, K. Amine and J. Lu, *Energy Storage Materials*, 2020, **28**, 73-81.
16. H. Yu, D. Liu, X. Feng and Y. Zhang, *Energy & Fuels*, 2021, **35**, 4751-4761.
17. C. Wang, K. Fu, S. P. Kammampata, D. W. McOwen, A. J. Samson, L. Zhang, G. T. Hitz, A. M. Nolan,

E. D. Wachsman, Y. Mo, V. Thangadurai and L. Hu, *Chem Rev*, 2020, **120**, 4257-4300.
18. K. Chen, D.-Y. Yang, G. Huang and X.-B. Zhang, *Accounts of Chemical Research*, 2021, **54**, 632-641.
19. V. Rai, K. P. Lee, D. Safanama, S. Adams and D. J. Blackwood, *ACS Applied Energy Materials*, 2020, **3**, 9417-9427.
20. Y. C. Lu, H. A. Gasteiger and Y. Shao-Horn, *J Am Chem Soc*, 2011, **133**, 19048-19051.
21. S. Song, X. Qin, Y. Ruan, W. Li, Y. Xu, D. Zhang and J. Thokchom, *Journal of Power Sources*, 2020, **461**, 228146.
22. G. Wang, Y. Deng, J. Yu, L. Zheng, L. Du, H. Song and S. Liao, *ACS Appl Mater Interfaces*, 2017, **9**, 32168-32178.
23. Z. Chang, J. Xu and X. Zhang, *Advanced Energy Materials*, 2017, **7**, 1700875.
24. J. Wang, J. Zheng and X. Liu, *Physical Chemistry Chemical Physics*, 2022, **24**, 17920-17940.
25. W. B. Luo, X. W. Gao, D. Q. Shi, S. L. Chou, J. Z. Wang and H. K. Liu, *Small*, 2016, **12**, 3031-3038.
26. J. Pérez-Ramírez and N. López, *Nature Catalysis*, 2019, **2**, 971-976.
27. B. Huang, W. Zhang, J. Chen, Y. Cui, C. Zhu and S. Yan, *Journal of The Electrochemical Society*, 2023, **170**, 020506.
28. R. Sharma, H. Kumar, G. Kumar, S. Sharma, R. Aneja, A. K. Sharma, R. Kumar and P. Kumar, *Chemical Engineering Journal*, 2023, **468**, 143706.
29. G. Yue, Z. Hong, Y. Xia, T. Yang and Y. Wu, *Coatings*, 2022, **12**, 1227.
30. X. Lv, M. Chen, H. Kimura, W. Du and X. Yang, *International Journal of Molecular Sciences*, 2023, **24**, 3713.
31. Y. Dou, D. Kan, Y. Su, Y. Zhang, Y. Wei, Z. Zhang and Z. Zhou, *The Journal of Physical Chemistry Letters*, 2022, **13**, 7081-7086.
32. Y. Dou, Z. Xie, Y. Wei, Z. Peng and Z. Zhou, *National Science Review*, 2022, **9**, nwac040.
33. L. Du, L. Xing, G. Zhang and S. Sun, *Carbon*, 2020, **156**, 77-92.
34. D. Wang, X. Mu, P. He and H. Zhou, *Materials Today*, 2019, **26**, 87-99.
35. A. Tan, M. V. Reddy and S. Adams, *Ionics*, 2017, **23**, 2589-2602.
36. J. Zhang, C. Si, T. Kou, J. Wang and Z. Zhang, *Sustainable Energy & Fuels*, 2020, **4**, 2625-2637.
37. H.-D. Lim, B. Lee, Y. Bae, H. Park, Y. Ko, H. Kim, J. Kim and K. Kang, *Chemical Society Reviews*, 2017, **46**, 2873-2888.
38. D. Geng, N. Ding, T. S. A. Hor, S. W. Chien, Z. Liu, D. Wuu, X. Sun and Y. Zong, *Advanced Energy Materials*, 2016, **6**, 1502164.
39. X. Xu, W. Liu, Y. Kim and J. Cho, *Nano Today*, 2014, **9**, 604-630.
40. D. Cao, Y. Bai, J. Zhang, G. Tan and C. Wu, *Nano Energy*, 2021, **89**, 106464.
41. C. Liu, X. Han, Y. Cao, S. Zhang, Y. Zhang and J. Sun, *Energy Storage Materials*, 2019, **20**, 343-372.
42. Y. Wang and Y. C. Lu, *Energy Storage Materials*, 2020, **28**, 235-246.
43. M. Ren, J. Chen, G. Wu, E. A. McHugh, A.-L. Tsai and J. M. Tour, *ACS Catalysis*, 2021, **11**, 1833-1840.
44. D. Ahuja, V. Kalpna and P. K. Varshney, *Journal of Physics: Conference Series*, 2021, **1913**, 012065.
45. Z. Q. Peng, S. A. Freunberger, L. J. Hardwick, Y. H. Chen, V. Giordani, F. Barde, P. Novak, D. Graham, J. M. Tarascon and P. G. Bruce, *Angewandte Chemie-International Edition*, 2011, **50**, 6351-6355.
46. N. Mozhzhukhina, L. P. Méndez De Leo and E. J. Calvo, *The Journal of Physical Chemistry C*, 2013, **117**, 18375-18380.
47. Z. Wang, B. Huang, S. Wang, R. Xue, X. Huang and L. Chen, *Electrochimica Acta*, 1997, **42**, 2611-

2617.
48. D. Lee, H. Park, Y. Ko, H. Park, T. Hyeon, K. Kang and J. Park, *J Am Chem Soc*, 2019, **141**, 8047-8052.
49. P. Sabatier, *Berichte der deutschen chemischen Gesellschaft*, 1911, **44**, 1984-2001.
50. M. Busch, N. B. Halck, U. I. Kramm, S. Siahrostami, P. Krtil and J. Rossmeisl, *Nano Energy*, 2016, **29**, 126-135.
51. M. T. M. Koper, *Topics in Catalysis*, 2015, **58**, 1153-1158.
52. M. Sevim, T. Şener and Ö. Metin, *International Journal of Hydrogen Energy*, 2015, **40**, 10876-10882.
53. L. Leng, J. Li, X. Zeng, H. Song, T. Shu, H. Wang and S. Liao, *Journal of Power Sources*, 2017, **337**, 173-179.
54. Y.-J. Kang, S. C. Jung, H.-J. Kim, Y.-K. Han and S. H. Oh, *Nano Energy*, 2016, **27**, 1-7.
55. X. Ren, B. Liao, Y. Li, P. Zhang, L. Deng and Y. Gao, *Electrochimica Acta*, 2017, **228**, 36-44.
56. D. Su, H.-S. Kim, W.-S. Kim and G. Wang, *Journal of Power Sources*, 2013, **244**, 488-493.
57. H. Lv, L. Lin, X. Zhang, Y. Song, H. Matsumoto, C. Zeng, N. Ta, W. Liu, D. Gao, G. Wang and X. Bao, *Adv Mater*, 2020, **32**, e1906193.
58. R. Choi, J. Jung, G. Kim, K. Song, Y.-I. Kim, S. C. Jung, Y.-K. Han, H. Song and Y.-M. Kang, *Energy & Environmental Science*, 2014, **7**, 1362-1368.
59. J. Wang, L. Liu, S. Chou, H. Liu and J. Wang, *Journal of Materials Chemistry A*, 2017, **5**, 1462-1471.
60. X. Hu, J. Shi, J. Zhang, W. Tang, H. Zhu, X. Shen and N. Saito, *Journal of Alloys and Compounds*, 2015, **619**, 452-457.
61. M. Lee, Y. Hwang, K.-H. Yun and Y.-C. Chung, *Journal of Power Sources*, 2015, **288**, 296-301.
62. M. Luo, Z. Zhao, Y. Zhang, Y. Sun, Y. Xing, F. Lv, Y. Yang, X. Zhang, S. Hwang, Y. Qin, J. Y. Ma, F. Lin, D. Su, G. Lu and S. Guo, *Nature*, 2019, **574**, 81-85.
63. Y. Cong, Z. Geng, Q. Zhu, H. Hou, X. Wu, X. Wang, K. Huang and S. Feng, *Angew Chem Int Ed Engl*, 2021, **60**, 23380-23387.
64. H. Wang, F. Yin, P. Lv, T. Fan, X. He and B. Chen, *International Journal of Hydrogen Energy*, 2017, **42**, 2127-2133.
65. X. Ren, M. Huang, S. Luo, Y. Li, L. Deng, H. Mi, L. Sun and P. Zhang, *Journal of Materials Chemistry A*, 2018, **6**, 10856-10867.
66. Z. Chang, F. Yu, Z. Liu, S. Peng, M. Guan, X. Shen, S. Zhao, N. Liu, Y. Wu and Y. Chen, *ACS Appl Mater Interfaces*, 2020, **12**, 4366-4372.
67. C. Z. Shu, J. Z. Wang, J. P. Long, H. K. Liu and S. X. Dou, *Advanced Materials*, 2019, **31**.
68. D. A. Agyeman, Y. Zheng, T.-H. Lee, M. Park, W. Tamakloe, G.-H. Lee, H. W. Jang, K. Cho and Y.-M. Kang, *ACS Catalysis*, 2020, **11**, 424-434.
69. B. Liu, Y. Sun, L. Liu, S. Xu and X. Yan, *Advanced Functional Materials*, 2018, **28**, 1704973.
70. Z. L. Wang, D. Xu, J. J. Xu and X. B. Zhang, *Chem Soc Rev*, 2014, **43**, 7746-7786.
71. E. Pargoletti, A. Salvi, A. Giordana, G. Cerrato, M. Longhi, A. Minguzzi, G. Cappelletti and A. Vertova, *Journal*, 2020, **10**, 1735.
72. J. Pan, X. L. Tian, S. Zaman, Z. Dong, H. Liu, H. S. Park and B. Y. Xia, *Batteries & Supercaps*, 2018, **2**, 336-347.
73. G. Wang, L. Huang, W. Huang, J. Xie, G. Du, S. Zhang, P. Zhu, G. Cao and X. Zhao, *Nanoscale*, 2015, **7**, 20614-20624.
74. X. Lang, F. Ge, K. Cai, L. Li, Q. Wang and Q. Zhang, *Journal of Alloys and Compounds*, 2019, **770**, 451-457.

75. M. Balaish, J.-W. Jung, I.-D. Kim and Y. Ein-Eli, *Advanced Functional Materials*, 2020, **30**, 1808303.
76. J. A. Dawson and I. Tanaka, *ACS Appl Mater Interfaces*, 2015, **7**, 8125-8131.
77. Y. Hang, C. Zhang, X. Luo, Y. Xie, S. Xin, Y. Li, D. Zhang and J. B. Goodenough, *Journal of Power Sources*, 2018, **392**, 15-22.
78. T. A. Mellan, K. P. Maenetja, P. E. Ngoepe, S. M. Woodley, C. R. A. Catlow and R. Grau-Crespo, *Journal of Materials Chemistry A*, 2013, **1**, 14879-14887.
79. F. Cheng, Y. Su, J. Liang, Z. Tao and J. Chen, *Chemistry of Materials*, 2009, **22**, 898-905.
80. X. Hu, F. Cheng, X. Han, T. Zhang and J. Chen, *Small*, 2015, **11**, 809-813.
81. J. Zhang, Y. Luan, Z. Lyu, L. Wang, L. Xu, K. Yuan, F. Pan, M. Lai, Z. Liu and W. Chen, *Nanoscale*, 2015, **7**, 14881-14888.
82. X. Hu, J. Wang, Z. Li, J. Wang, D. H. Gregory and J. Chen, *Nano Lett*, 2017, **17**, 2073-2078.
83. X. Hu, F. Cheng, N. Zhang, X. Han and J. Chen, *Small*, 2015, **11**, 5545-5550.
84. A. Minguzzi, G. Longoni, G. Cappelletti, E. Pargoletti, C. Di Bari, C. Locatelli, M. Marelli, S. Rondinini and A. Vertova, *Nanomaterials*, 2016, **6**, 10.
85. W. B. Luo, S. L. Chou, W. Jia-Zhao, Y. C. Zhai and H. K. Liu, *Sci Rep*, 2015, **5**, 8012.
86. A. K. Thapa and T. Ishihara, *Journal of Power Sources*, 2011, **196**, 7016-7020.
87. A. K. Thapa, T. H. Shin, S. Ida, G. U. Sumanasekera, M. K. Sunkara and T. Ishihara, *Journal of Power Sources*, 2012, **220**, 211-216.
88. D. Oh, J. Qi, Y. C. Lu, Y. Zhang, Y. Shao-Horn and A. M. Belcher, *Nat Commun*, 2013, **4**, 2756.
89. M. Alaf, U. Tocoglu, M. Kartal and H. Akbulut, *Applied Surface Science*, 2016, **380**, 185-192.
90. H. Jang, A. Zahoor, J. S. Jeon, P. Kim, Y. S. Lee and K. S. Nahm, *Journal of The Electrochemical Society*, 2014, **162**, A300-A307.
91. Y.-F. Xu, Y. Chen, G.-L. Xu, X.-R. Zhang, Z. Chen, J.-T. Li, L. Huang, K. Amine and S.-G. Sun, *Nano Energy*, 2016, **28**, 63-70.
92. Y. Dou, X.-G. Wang, D. Wang, Q. Zhang, C. Wang, G. Chen, Y. Wei and Z. Zhou, *Chemical Engineering Journal*, 2021, **409**, 128145.
93. C. Tang, P. Sun, J. Xie, Z. Tang, Z. Yang, Z. Dong, G. Cao, S. Zhang, P. V. Braun and X. Zhao, *Energy Storage Materials*, 2017, **9**, 206-213.
94. F. Wang, Z. Wen, C. Shen, X. Wu and J. Liu, *Phys Chem Chem Phys*, 2016, **18**, 926-931.
95. C. Cao, J. Xie, S. Zhang, B. Pan, G. Cao and X. Zhao, *Journal of Materials Chemistry A*, 2017, **5**, 6747-6755.
96. J. Li, Z. Wang, L. Yang, Y. Liu, Y. Xing, S. Zhang and H. Xu, *ACS Appl Mater Interfaces*, 2021, **13**, 18627-18637.
97. B. He, J. Wang, J. Liu, Y. Li, Q. Huang, Y. Hou, G. Li, J. Li, R. Zhang, J. Zhou, W. Tian, Y. Du, F. Dang, H. Wang and B. Kong, *Advanced Energy Materials*, 2020, **10**, 1904262.
98. J. Zhu, X. Ren, J. Liu, W. Zhang and Z. Wen, *ACS Catalysis*, 2014, **5**, 73-81.
99. H.-C. Li, Y.-J. Zhang, X. Hu, W.-J. Liu, J.-J. Chen and H.-Q. Yu, *Advanced Energy Materials*, 2018, **8**, 1702734.
100. T. Ling, D. Y. Yan, Y. Jiao, H. Wang, Y. Zheng, X. Zheng, J. Mao, X. W. Du, Z. Hu, M. Jaroniec and S. Z. Qiao, *Nat Commun*, 2016, **7**, 12876.
101. P. W. Menezes, A. Indra, N. R. Sahraie, A. Bergmann, P. Strasser and M. Driess, *ChemSusChem*, 2015, **8**, 164-171.
102. Y. Cui, Z. Wen and Y. Liu, *Energy & Environmental Science*, 2011, **4**, 4727-4734.
103. Y. J. Sa, K. Kwon, J. Y. Cheon, F. Kleitz and S. H. Joo, *Journal of Materials Chemistry A*, 2013, **1**,

9992-10001.

104. C. Cao, Y. Yan, H. Zhang, J. Xie, S. Zhang, B. Pan, G. Cao and X. Zhao, *ACS Appl Mater Interfaces*, 2016, **8**, 31653-31660.
105. H. M. A. Amin, C. J. Bondue, S. Eswara, U. Kaiser and H. Baltruschat, *Electrocatalysis*, 2017, **8**, 540-553.
106. R. Gao, Z. Yang, L. Zheng, L. Gu, L. Liu, Y. Lee, Z. Hu and X. Liu, *ACS Catalysis*, 2018, **8**, 1955-1963.
107. C. Li, D. Liu, Y. Xiao, Z. Liu, L. Song and Z. Zhang, *ACS Applied Energy Materials*, 2019, **2**, 2939-2947.
108. W. Sun, Y. Wang, H. Wu, Z. Wang, D. Rooney and K. Sun, *Chem Commun (Camb)*, 2017, **53**, 8711-8714.
109. Y. J. Yun, J. K. Kim, J. Y. Ju, S. Unithrattil, S. S. Lee, Y. Kang, H. K. Jung, J. S. Park, W. B. Im and S. Choi, *Dalton Trans*, 2016, **45**, 5064-5070.
110. S. Peng, Y. Hu, L. Li, X. Han, F. Cheng, M. Srinivasan, Q. Yan, S. Ramakrishna and J. Chen, *Nano Energy*, 2015, **13**, 718-726.
111. H. Wu, W. Sun, Y. Wang, F. Wang, J. Liu, X. Yue, Z. Wang, J. Qiao, D. W. Rooney and K. Sun, *ACS Appl Mater Interfaces*, 2017, **9**, 12355-12365.
112. S. G. Mohamed, Y. Q. Tsai, C. J. Chen, Y. T. Tsai, T. F. Hung, W. S. Chang and R. S. Liu, *ACS Appl Mater Interfaces*, 2015, **7**, 12038-12046.
113. X. Tao, J. Du, Y. Yang, Y. Li, Y. Xia, Y. Gan, H. Huang, W. Zhang and X. Li, *Crystal Growth & Design*, 2011, **11**, 4422-4426.
114. A. Y. Kozmenkova, E. Y. Kataev, A. I. Belova, M. Amati, L. Gregoratti, J. Velasco-Vélez, A. Knop-Gericke, B. Senkovsky, D. V. Vyalikh, D. M. Itkis, Y. Shao-Horn and L. V. Yashina, *Chemistry of Materials*, 2016, **28**, 8248-8255.
115. C. Liu, Z. Qiu, W. R. Brant, R. Younesi, Y. Ma, K. Edström, T. Gustafsson and J. Zhu, *Journal of Materials Chemistry A*, 2018, **6**, 23659-23668.
116. M. M. Ottakam Thotiyl, S. A. Freunberger, Z. Peng, Y. Chen, Z. Liu and P. G. Bruce, *Nat Mater*, 2013, **12**, 1050-1056.
117. X. Feng, K. Zhu, A. J. Frank, C. A. Grimes and T. E. Mallouk, *Angew Chem Int Ed Engl*, 2012, **51**, 2727-2730.
118. S. Cao, Z. Xue, C. Yang, J. Qin, L. Zhang, P. Yu, S. Wang, Y. Zhao, X. Zhang and R. Liu, *Nano Energy*, 2018, **50**, 25-34.
119. B. D. Adams, R. Black, C. Radtke, Z. Williams, B. L. Mehdi, N. D. Browning and L. F. Nazar, *Acs Nano*, 2014, **8**, 12483-12493.
120. M.-G. Jeong, W.-J. Kwak, H.-J. Shin, Y.-K. Sun and H.-G. Jung, *Chemical Engineering Journal*, 2020, **399**, 125699.
121. F. Li, R. Ohnishi, Y. Yamada, J. Kubota, K. Domen, A. Yamada and H. Zhou, *Chem Commun (Camb)*, 2013, **49**, 1175-1177.
122. B. G. Kim, C. Jo, J. Shin, Y. Mun, J. Lee and J. W. Choi, *ACS Nano*, 2017, **11**, 1736-1746.
123. V. Molinari, C. Giordano, M. Antonietti and D. Esposito, *J Am Chem Soc*, 2014, **136**, 1758-1761.
124. L. Leng, J. Li, X. Zeng, X. Tian, H. Song, Z. Cui, T. Shu, H. Wang, J. Ren and S. Liao, *Nanoscale*, 2018, **10**, 2983-2989.
125. X. Tian, J. Luo, H. Nan, H. Zou, R. Chen, T. Shu, X. Li, Y. Li, H. Song, S. Liao and R. R. Adzic, *J Am Chem Soc*, 2016, **138**, 1575-1583.

126. W. B. Luo, T. V. Pham, H. P. Guo, H. K. Liu and S. X. Dou, *ACS Nano*, 2017, **11**, 1747-1754.
127. Z. Ma, X. Yuan, Z. Zhang, D. Mei, L. Li, Z.-F. Ma, L. Zhang, J. Yang and J. Zhang, *Scientific Reports*, 2015, **5**, 18199.
128. P. Sennu, M. Christy, V. Aravindan, Y.-G. Lee, K. S. Nahm and Y.-S. Lee, *Chemistry of Materials*, 2015, **27**, 5726-5735.
129. Q. Wang, X. Wang and H. He, *Journal of Power Sources*, 2020, **448**, 227397.
130. S. Ding, S. Liu, J. Li, L. Wu, Z.-F. Ma and X. Yuan, *ACS Applied Materials & Interfaces*, 2021, **13**, 50065-50075.
131. A. Hu, J. Long, C. Shu, R. Liang and J. Li, *ACS Applied Materials & Interfaces*, 2018, **10**, 34077-34086.
132. X. Lin, R. Yuan, S. Cai, Y. Jiang, J. Lei, S.-G. Liu, Q.-H. Wu, H.-G. Liao, M. Zheng and Q. Dong, *Advanced Energy Materials*, 2018, **8**, 1800089.
133. P. Ramakrishnan, S. Shanmugam and J. H. Kim, *ChemSusChem*, 2017, **10**, 1554-1562.
134. C. Han, Q. Li, D. Wang, Q. Lu, Z. Xing and X. Yang, *Small*, 2018, **14**, 1703642.
135. L. Li, L. Song, H. Guo, W. Xia, C. Jiang, B. Gao, C. Wu, T. Wang and J. He, *Nanoscale*, 2019, **11**, 901-907.
136. Y. Cao, H. Lu, B. Xu, W. Yang and Q. Hong, *Chemical Engineering Journal*, 2019, **378**, 122247.
137. S. Ding, L. Wu, F. Zhang and X. Yuan, *Small*, 2023, **19**, 2300602.
138. C. Cheng, X. Zhang, C. Wei, Y. Liu, C. Cui, Q. Zhang and D. Zhang, *Ceramics International*, 2018, **44**, 17464-17472.
139. S. Li, J. Xu, Z. Ma, S. Zhang, X. Wen, X. Yu, J. Yang, Z.-F. Ma and X. Yuan, *Chemical Communications*, 2017, **53**, 8164-8167.
140. A. Hu, J. Long, C. Shu, C. Xu, T. Yang, R. Liang and J. Li, *Electrochimica Acta*, 2019, **301**, 69-79.
141. J. Wang, R. Zhan, Y. Fu, H.-Y. Yu, C. Jiang, T.-H. Zhang, C. Zhang, J. Yao, J.-F. Li, X. Li, J.-H. Tian and R. Yang, *Materials Today Energy*, 2017, **5**, 214-221.
142. M. Xu, S. Ding, X. Yu, Z.-F. Ma and X. Yuan, *ACS Applied Energy Materials*, 2022, **5**, 10415-10426.
143. S. Hyun, B. Son, H. Kim, J. Sanetuntikul and S. Shanmugam, *Applied Catalysis B: Environmental*, 2020, **263**, 118283.
144. H. Cui, Z. Zhou and D. Jia, *Materials Horizons*, 2017, **4**, 7-19.
145. W. Li, C. Han, K. Zhang, S. Chou and S. Dou, *Journal of Materials Chemistry A*, 2021, **9**, 6671-6693.
146. R. Mi, S. Li, X. Liu, L. Liu, Y. Li, J. Mei, Y. Chen, H. Liu, H. Wang, H. Yan and W.-M. Lau, *J. Mater. Chem. A*, 2014, **2**, 18746-18753.
147. Z. Lyu, L. Yang, Y. Luan, X. Renshaw Wang, L. Wang, Z. Hu, J. Lu, S. Xiao, F. Zhang, X. Wang, F. Huo, W. Huang, Z. Hu and W. Chen, *Nano Energy*, 2017, **36**, 68-75.
148. Y. Huang, Y. Wang, C. Tang, J. Wang, Q. Zhang, Y. Wang and J. Zhang, *Advanced Materials*, 2019, **31**, 1803800.
149. X. Zhang, X. Xu, S. Yao, C. Hao, C. Pan, X. Xiang, Z. Q. Tian, P. K. Shen, Z. Shao and S. P. Jiang, *Small*, 2022, **18**, 2105329.
150. Z. Kou, B. Guo, D. He, J. Zhang and S. Mu, *ACS Energy Letters*, 2017, **3**, 184-190.
151. I.-Y. Jeon, S. Zhang, L. Zhang, H.-J. Choi, J.-M. Seo, Z. Xia, L. Dai and J.-B. Baek, *Advanced Materials*, 2013, **25**, 6138-6145.
152. S. Yang, Y. Zhan, J. Li and J. Y. Lee, *ACS Appl Mater Interfaces*, 2016, **8**, 3535-3542.
153. J.-H. Kim, A. G. Kannan, H.-S. Woo, D.-G. Jin, W. Kim, K. Ryu and D.-W. Kim, *Journal of Materials Chemistry A*, 2015, **3**, 18456-18465.

154. J. Zhang and L. Dai, *Angewandte Chemie International Edition*, 2016, **55**, 13296-13300.
155. N. E. Benti, G. A. Tiruye and Y. S. Mekonnen, *RSC Advances*, 2020, **10**, 21387-21398.
156. Y.-C. Yin, R.-X. Deng, D.-R. Yang, Y.-B. Sun, Z.-Q. Li and X.-H. Xia, *The Journal of Physical Chemistry Letters*, 2022, **13**, 4350-4356.
157. D. Wu, S. Wu, G. Zhang, C. Hui, D. Cao, S. Guo, H. Feng, Q. Wang, S. Cheng, P. Cui and Z. Yang, *Small*, 2023, DOI: 10.1002/smll.202206455, e2206455.
158. Z. Guo, D. Zhou, X. Dong, Z. Qiu, Y. Wang and Y. Xia, *Advanced Materials*, 2013, **25**, 5668-5672.
159. K. H. Lim, S. Kim, H. Kweon, S. Moon, C. H. Lee and H. Kim, *Journal of Materials Chemistry A*, 2018, **6**, 4040-4047.
160. Z.-L. Jiang, H. Sun, W.-K. Shi, J.-Y. Cheng, J.-Y. Hu, H.-L. Guo, M.-Y. Gao, H. Zhou and S.-G. Sun, *ACS Sustainable Chemistry & Engineering*, 2019, **7**, 14161-14169.
161. H. Huang, C. Cheng, G. Zhang, L. Guo, G. Li, M. Pan, F. Dang and X. Mai, *Advanced Functional Materials*, 2022, **32**, 2111546.
162. M. Liu, X. Zhu, Y. Song, G. Huang, J. Wei, X. Song, Q. Xiao, T. Zhao, W. Jiang, X. Li and W. Luo, *Advanced Functional Materials*, 2023, **33**, 2213395.
163. Y. Liu, P. He and H. Zhou, *Advanced Energy Materials*, 2018, **8**, 1701602.
164. Y. Guo, H. Li and T. Zhai, *Advanced Materials*, 2017, **29**, 1700007.
165. H. Wang, M. Matsui, H. Kuwata, H. Sonoki, Y. Matsuda, X. Shang, Y. Takeda, O. Yamamoto and N. Imanishi, *Nat Commun*, 2017, **8**, 15106.
166. B. Liu, J.-G. Zhang and W. Xu, *Joule*, 2018, **2**, 833-845.
167. D. Lin, Y. Liu, Z. Liang, H. W. Lee, J. Sun, H. Wang, K. Yan, J. Xie and Y. Cui, *Nat Nanotechnol*, 2016, **11**, 626-632.
168. W. Xu, J. Wang, F. Ding, X. Chen, E. Nasybulin, Y. Zhang and J.-G. Zhang, *Energy Environ. Sci.*, 2014, **7**, 513-537.
169. R. Pathak, K. Chen, A. Gurung, K. M. Reza, B. Bahrami, J. Pokharel, A. Baniya, W. He, F. Wu and Y. Zhou, *Nature communications*, 2020, **11**, 93.
170. R. Pathak, K. Chen, A. Gurung, K. M. Reza, B. Bahrami, F. Wu, A. Chaudhary, N. Ghimire, B. Zhou and W. H. Zhang, *Advanced Energy Materials*, 2019, **9**, 1901486.
171. K. Chen, R. Pathak, A. Gurung, E. A. Adhamash, B. Bahrami, Q. He, H. Qiao, A. L. Smirnova, J. J. Wu and Q. Qiao, *Energy Storage Materials*, 2019, **18**, 389-396.
172. A. Baniya, A. Gurung, J. Pokharel, K. Chen, R. Pathak, B. S. Lamsal, N. Ghimire, R. S. Bobba, S. I. Rahman and S. Mabrouk, *ACS Applied Energy Materials*, 2022, **5**, 648-657.
173. K. Chen, R. Pathak, A. Gurung, K. M. Reza, N. Ghimire, J. Pokharel, A. Baniya, W. He, J. J. Wu and Q. Q. Qiao, *Journal of Materials Chemistry A*, 2020, **8**, 1911-1919.
174. W. Li, H. Yao, K. Yan, G. Zheng, Z. Liang, Y.-M. Chiang and Y. Cui, *Nature communications*, 2015, **6**, 7436.
175. S. Qi, J. He, J. Liu, H. Wang, M. Wu, F. Li, D. Wu, X. Li and J. Ma, *Advanced Functional Materials*, 2021, **31**, 2009013.
176. A. Baniya, R. Pathak, B. Norris, H. Li, V. Rozyyev, J. W. Elam and Q. Qiao, in *Green Sustainable Process for Chemical and Environmental Engineering and Science*, Elsevier, 2023, pp. 1-46.
177. J. Y. Kim, D. O. Shin, K. M. Kim, J. Oh, J. Kim, S. H. Kang, M. J. Lee and Y.-G. Lee, *Scientific Reports*, 2019, **9**, 2464.
178. B. Boateng, X. Zhang, C. Zhen, D. Chen, Y. Han, C. Feng, N. Chen and W. He, *Nano Select*, 2021, **2**, 993-1010.

179. J.-J. Xu, Q.-C. Liu, Y. Yu, J. Wang, J.-M. Yan and X.-B. Zhang, *Advanced Materials*, 2017, **29**, 1606552.
180. C. Yan, X. B. Cheng, Y. Tian, X. Chen, X. Q. Zhang, W. J. Li, J. Q. Huang and Q. Zhang, *Adv Mater*, 2018, **30**, e1707629.
181. X. Zhang, Q. Zhang, X. G. Wang, C. Wang, Y. N. Chen, Z. Xie and Z. Zhou, *Angew Chem Int Ed Engl*, 2018, **57**, 12814-12818.
182. K. Chen, R. Pathak, W. He and Y. Zhou, in *Green Sustainable Process for Chemical and Environmental Engineering and Science*, Elsevier, 2023, pp. 81-94.
183. S.-S. Chi, Y. Liu, W.-L. Song, L.-Z. Fan and Q. Zhang, *Advanced Functional Materials*, 2017, **27**, 1700348.
184. J. Lai, Y. Xing, N. Chen, L. Li, F. Wu and R. Chen, *Angew Chem Int Ed Engl*, 2020, **59**, 2974-2997.
185. H. Zhang, G. G. Eshetu, X. Judez, C. Li, L. M. Rodriguez-Martinez and M. Armand, *Angew Chem Int Ed Engl*, 2018, **57**, 15002-15027.
186. S. Wang, J. Wang, J. Liu, H. Song, Y. Liu, P. Wang, P. He, J. Xu and H. Zhou, *Journal of Materials Chemistry A*, 2018, **6**, 21248-21254.
187. H. Liao, H. Chen, F. Zhou, Z. Zhang and H. Chen, *Journal of Power Sources*, 2019, **435**, 226748.
188. T. Zhang and H. Zhou, *Nat Commun*, 2013, **4**, 1817.
189. S. H. Choi, J. Kim and Y. S. Yoon, *Journal of Power Sources*, 2004, **135**, 286-290.
190. J. Yi, S. Guo, P. He and H. Zhou, *Energy & Environmental Science*, 2017, **10**, 860-884.
191. S. Wu, J. Yi, K. Zhu, S. Bai, Y. Liu, Y. Qiao, M. Ishida and H. Zhou, *Advanced Energy Materials*, 2017, **7**, 1601759.
192. A. Kondori, M. Esmaeilirad, A. M. Harzandi, R. Amine, M. T. Saray, L. Yu, T. Liu, J. Wen, N. Shan, H.-H. Wang, A. T. Ngo, P. C. Redfern, C. S. Johnson, K. Amine, R. Shahbazian-Yassar, L. A. Curtiss and M. Asadi, *Science*, 2023, **379**, 499-505.
193. S. Wu, J. Yi, K. Zhu, S. Bai, Y. Liu, Y. Qiao, M. Ishida and H. Zhou, *Advanced Energy Materials*, 2017, **7**.
194. F. Li, T. Zhang, Y. Yamada, A. Yamada and H. Zhou, *Advanced Energy Materials*, 2013, **3**, 532-538.
195. S.-S. Chi, Y. Liu, N. Zhao, X. Guo, C.-W. Nan and L.-Z. Fan, *Energy Storage Materials*, 2019, **17**, 309-316.
196. C.-N. Wei, C. Karuppiah, C.-C. Yang, J.-Y. Shih and S. J. Lue, *Journal of Physics and Chemistry of Solids*, 2019, **133**, 67-78.
197. M. Xie, Z. Huang, X. Lin, Y. Li, Z. Huang, L. Yuan, Y. Shen and Y. Huang, *Energy Storage Materials*, 2019, **20**, 307-314.
198. S. H. Lee, J. R. Harding, D. S. Liu, J. M. D'Arcy, Y. Shao-Horn and P. T. Hammond, *Chemistry of Materials*, 2014, **26**, 2579-2585.